

# Thermal diffusion in polymer blends: criticality and pattern formation

W. Köhler, A. Krekhov, and W. Zimmermann

**Abstract** We have determined the dynamic critical properties of a binary blend of the two polymers poly(dimethyl siloxane) (PDMS) and poly(ethyl-methyl siloxane) (PEMS), and we have investigated experimentally and theoretically patterning and structure formation processes above and below the spinodal in the case of a spatially varying temperature. Ising-like scaling is found for the asymptotic critical regime close to  $T_c$  in the range  $6 \times 10^{-4} \leq \varepsilon \leq 0.2$  of the reduced temperature  $\varepsilon$  and a mean field behavior for large values of  $\varepsilon$ . The thermal diffusion coefficient  $D_T$  is thermally activated but does not show the critical slowing down of the Fickian diffusion coefficient  $D$ , which can be described by crossover functions for  $D$ . The Soret coefficient  $S_T = D_T/D$  diverges at the critical point with a critical exponent  $-0.67$  and shows a crossover to the exponent  $-1$  of the structure factor in the classical regime. Thermal activation processes cancel out and do not contribute to  $S_T$ . The divergence of  $S_T$  leads to a very strong coupling of the order parameter also to small temperature gradients, which can be utilized for laser patterning of thin polymer films. For a quantitative numerical model all three coefficients  $D$ ,  $D_T$ , and  $S_T$  have been determined within the entire homogeneous phase and are parameterized by a pseudospinodal model. It is shown that equilibrium phase diagrams are no longer globally valid in the presence of a temperature gradient, and systems with an upper critical solution temperature (UCST) can be quenched into phase separation by local heating. Below the spinodal there is a competition between the spontaneous spinodal demixing patterns and structures imposed by means of a focused laser beam utilizing the Soret effect. Elongated structures degrade to spherical objects due to surface tension effects leading to pearling instabilities. Grids of parallel lines can be

---

W. Köhler

Physikalisches Institut, Universität Bayreuth, e-mail: werner.koehler@uni-bayreuth.de

A. Krekhov

Physikalisches Institut, Universität Bayreuth, e-mail: alexei.krekhov@uni-bayreuth.de

W. Zimmermann

Physikalisches Institut, Universität Bayreuth, e-mail: walter.zimmermann@uni-bayreuth.de

stabilized by enforcing certain boundary conditions. Phase separation phenomena in polymer blends count to the universality class of pattern forming systems with a conserved order parameter. In such systems, the effects of spatial forcing are rather unexplored and, as described in this work, spatial temperature modulations may cause via the Soret effect (thermal diffusion) a variety of interesting concentration modulations. In the framework of a generalized Cahn-Hilliard model it is shown that coarsening in the two-phase range of phase separating systems can be interrupted by a spatially periodic temperature modulation with a modulation amplitude beyond a critical one, where in addition the concentration modulations are locked to the periodicity of the external forcing. Accordingly, temperature modulations may be a useful future tool for controlled structuring of polymer blends. In the case of a traveling spatially periodic forcing, but with a modulation amplitude below the critical one, the coarsening dynamics can be enhanced. With a model of phase separation, taking into account thermal diffusion, essential features of the spatio-temporal dynamics of phase separation and thermal patterning observed in experiments can be reproduced. With a directional quenching an effective approach is studied to create regular structures during the phase separation process. In addition, it is shown that the wavelength of periodic stripe patterns is uniquely selected by the velocity of a quench interface. With a spatially periodic modulation of the quench interface itself also cellular patterns can be generated.

## 1 Introduction

When a binary liquid mixture approaches the consolute critical point, the equilibrium restoring forces vanish, the correlation length diverges and the amplitude of the fluctuations of the order parameter grow according to characteristic power laws. Very close to the critical point the correlation length exceeds by far all microscopic length scales. The fluctuations can be observed macroscopically as critical scattering phenomena like the well-known critical opalescence. At the same time there is a critical slowing down of the diffusion dynamics [1, 2, 3] and the system becomes increasingly susceptible to external perturbations.

After crossing the spinodal the mixture immediately becomes unstable and even arbitrarily small composition fluctuations grow exponentially in time. Eventually, the fluid decomposes into two phases that form a labyrinthine spinodal pattern with a characteristic length scale determined by the wave vector at the maximum of the growth rate of small inhomogeneous perturbations. As time proceeds the pattern coarsens and the maximum of the structure factor is shifted towards larger length scales, corresponding to smaller values of the wave vector. Eventually, a new equilibrium is reached with a horizontal meniscus that separates the two phases with the lighter liquid on top of the denser one.

Compared to binary mixtures of low molecular fluids, the critical behavior of polymer blends has been much less explored so far. However, a number of interesting static and dynamic critical phenomena in polymer blends attract increasing

attention [4, 5]. Neutron, X-ray, and static light scattering experiments belong to the major techniques for characterizing the static properties of polymer blends. Photon correlation spectroscopy (PCS) has traditionally been the method of choice for the investigation of the dynamics of critical [6, 7, 8, 9] and non-critical [10, 11, 12] polymer blends.

The vast majority of experimental and theoretical investigations on critical or off-critical polymer blends or solutions has been carried out under isothermal conditions and only a few of them were focusing on the effect of spatially varying temperature fields [13, 14, 15, 16, 17]. In all these studies there is no direct effect of a temperature gradient besides the positioning of the different parts of the sample at different locations in the phase diagram. The coupling between the order parameter and the temperature gradients due to the Ludwig-Soret effect – also termed thermal diffusion, thermodiffusion or, briefly, Soret effect – has not been taken into account. While this effect is only weak in most cases of low molecular mixtures away from a phase transition, it can, as will be shown below, become a substantial and sometimes dominating effect in critical polymer blends. The Soret coefficient, which is a measure for the change of the composition induced by a given temperature difference, even diverges at the critical point.

Including the Soret effect, the diffusive mass flow in a multicomponent system contains two contributions, the Fickian diffusion current that is driven by the gradient of the chemical potential and the thermal diffusion current driven by the temperature gradient. To account for this additional transport process, the thermal diffusion coefficient  $D_T$  is introduced in addition to the Fickian diffusion coefficient  $D$ . Experiments have shown that the direction of the thermal diffusion current is not easily predicted and in contrast to  $D$ , the coefficient  $D_T$  can be both positive and negative, and it can change its sign as a function of composition [18, 19, 20, 21, 22], temperature [23, 24, 25, 26], molar mass [27, 28] or solvent composition [29]. The stationary composition distribution is determined by a competition between thermal and Fickian diffusion, and the Soret coefficient  $S_T = D_T/D$  can roughly be interpreted as the relative composition change sustained in the stationary state by a prescribed temperature difference of 1 K. Typical numbers for small molecules are only of the order of  $S_T \approx 10^{-3} \text{ K}^{-1}$  and the effect generally causes only a minor perturbation for most practical situations. For larger diffusing species, such as polymers in dilute solution [30, 31, 32, 33] or colloids [34, 35, 36, 37, 38, 39, 40, 41], significantly higher values of  $S_T \approx 0.1 \dots 1 \text{ K}^{-1}$  have been reported.

The Soret effect near a consolute critical point of a simple liquid mixture was first investigated by Thomaes [42] and later by Giglio and Vendramini [43]. Giglio and Vendramini observed a critical divergence of the thermal diffusion factor  $k_T = S_T T c(1 - c) \sim (T - T_c)^\nu$  with the critical exponent  $\nu = 0.63$  of the correlation length  $\xi$ . These results, obtained with an optical beam deflection technique for the aniline/cyclohexane system, have later been confirmed by Wiegand utilizing a transient holographic grating technique [44]. Similar transient gratings had been used for the first time by Pohl to demonstrate qualitatively the divergence of the signal at the critical point of a 2,6-lutidine/water mixture [45]. Buil et al. and Delville et al. have employed transient holographic gratings [46] and focused laser

beams [47] for the investigation of first order phase transitions in multicomponent liquids. While there have been a few such studies of the Soret effect in critical low molecular weight liquid mixtures, there were no data available for critical polymer blends. Hence, one of the goals was the investigation of the critical properties related to non-isothermal transport, in particular the crossover from the mean field to the asymptotic critical regime, for a UCST polymer blend.

Besides the selection of a characteristic wavelength during spinodal decomposition at a constant temperature, the strong coupling between inhomogeneous temperature fields and the order parameter opens entirely new routes for pattern formation processes in critical polymer blends. Pattern formation in polymer blends via phase separation is an important research topic not only in polymer physics or physical chemistry but also as an interdisciplinary research involving nonequilibrium studies of complex fluids [48, 49], where it became a prototype for pattern forming systems with a conserved order parameter. The phase separation of such systems commonly leads to an isotropic, disordered morphology, such as interconnected domain structure or isolated clusters. These domains grow continuously in space and time and finally become macroscopic. An important research topic regarding phase separation in polymer blends is to fabricate regular structures for their potential application for nanotechnology in diverse fields, ranging from bioactive patterns [50] to polymer electronics [51]. In fact, polymer mixtures can undergo dramatic changes in response to externally applied perturbations. Some previous studies have considered the application of external fields, e.g., shear flow [52, 53], concentration gradient [54], patterned surface [55], temperature inhomogeneity [56], et al., to break the symmetry of the phase separation in polymer blends and to produce ordered structures with widely varying morphologies and length scales. Different strategies have been explored to tailor domain patterns of polymer mixtures and obtain new ordered structures. The spontaneous emergence of structures within an initially homogeneous blend and the possibility to generate patterns in a controlled way are not only of interest from the view of basic research but may also lead to technological applications.

Traditional techniques for structuring of polymer films utilize irradiation with UV light, X-rays or electron beams in combination with some kind of cross-linking photo reaction. Fytas and coworker have shown that isolated linear structures and periodic gratings can be generated by laser irradiation of homogeneous polymer solutions [57, 58]. Böltau et al. have used patterned surfaces to drive an incompatible polymer blend into pre-defined demixing morphologies [55]. Filler particles can induce composition waves in thin films of demixing polymer blends [59].

Spinodal decomposition in binary liquid mixture or polymer blends belongs to the universality class of pattern forming systems with a *conserved* order parameter [48]. A variety of interesting effects of spatially varying control parameters in pattern forming systems with *non-conserved* order parameters has been explored during the recent years [60, 61, 62, 63, 64, 65, 66, 67, 68, 69, 70, 71, 72, 73], but the effects of spatially or temporally varying temperature fields in spinodal decomposition has been investigated only recently. Tanaka and Sigehuzi have periodically driven the system across the spinodal and observed two characteristic superimposed length

scales with and without coarsening [74]. Lee et al. performed computational studies on spinodal decomposition with superimposed temperature gradient [17, 16]. Kumaki et al. observed a 20 K shift of the phase boundary after applying a temperature gradient to a ternary polymer mixture [75].

Except for Kumaki, all these authors did not take into account the coupling between temperature gradients and concentration due to the Soret effect. In the second part of the present work an overview of the structure formation processes is given that occur during spinodal decomposition in the presence of spatially inhomogeneous and/or time dependent temperature fields. It will be shown that the Soret effect may lead to entirely different pattern formation and evolution scenarios in critical and near-critical polymer blends. Introducing a spatially periodic temperature-modulation in a model of phase separation in a polymer blend above a critical modulation amplitude the coarsening dynamics can be interrupted and a stripe pattern is locked to the periodicity of the external modulation. Similar locking effects are found in the case of a traveling, spatially periodic temperature modulation. In the parameter range where the decomposition is not locked to the external forcing, the coarsening processes can be enhanced by the traveling modulation. With directional quenching a further forcing method is presented. This method turns out to be an effective selection mechanism for the wavelength of the periodic pattern behind the moving quenching interface, where the selected wavelength of the pattern can be uniquely selected by the chosen velocity of the quench interface.

## 2 Transport coefficients in a critical polymer blend

### 2.1 Diffusion in critical systems with a temperature gradient

At first we treat diffusion processes within the homogeneous phase. The presence of a temperature gradient in binary fluid mixtures and polymer blends requires an extension of Fick's diffusion laws, since the mass is not only driven by a concentration but also by a temperature gradient [76]:

$$\mathbf{J} = \mathbf{J}_m + \mathbf{J}_T = -\rho(D\nabla c + c(1-c)D_T\nabla T). \quad (1)$$

$c$  is the concentration (mass fraction),  $c\rho$  the density, and  $\mathbf{J}$  the mass flow of one component.  $D$  and  $D_T$  are the mass and the thermal diffusion coefficient, respectively. Since the total mass flow vanishes in the mass-fixed frame of reference, the flow of the second component of concentration  $1-c$  of the mixture is not independent and needs not be considered separately. In the case of vanishing reference velocities and/or small temperature gradients, the continuity equation takes the following form [77, 78]

$$\frac{\partial c}{\partial t} = -\nabla \cdot \frac{\mathbf{J}}{\rho}. \quad (2)$$

Combining Eqs. (1) and (2), the evolution equation for the concentration is

$$\frac{\partial c}{\partial t} = \nabla \cdot (D \nabla c + c(1-c) D_T \nabla T). \quad (3)$$

All currents vanish in the stationary state, where the amplitude of the induced concentration gradient is determined by the Soret coefficient  $S_T = D_T/D$ :

$$\nabla c = -S_T c(1-c) \nabla T \quad (4)$$

The temperature distribution is determined by the heat equation

$$\frac{\partial T}{\partial t} = D_{th} \nabla^2 T + S(\mathbf{r}, t), \quad (5)$$

including the source term  $S(\mathbf{r}, t)$ .  $D_{th} = \kappa(\rho c_p)^{-1}$  is the thermal diffusivity,  $\kappa$  the thermal conductivity, and  $c_p$  the specific heat of the solution.

The formal description of thermodiffusion in the critical region has been discussed in detail by Luettmmer-Strathmann [79]. The diffusion coefficient of a critical mixture in the long wavelength limit contains a mobility factor, the Onsager coefficient  $\alpha = \alpha^b + \Delta\alpha$ , and a thermodynamic contribution, the static structure factor  $S(0)$  [79, 7]:

$$D(q=0) = \left( \frac{\alpha^b + \Delta\alpha}{S(0)} \right) = D^b + \Delta D. \quad (6)$$

$\alpha^b$  is the background contribution and  $\Delta\alpha$  the critical enhancement. Within the random phase approximation the static structure factor of a binary A-B polymer blend is given by [8, 4, 80]

$$S(q=0) = \left( \frac{1}{\phi_A N_A} + \frac{1}{\phi_B N_B} - 2\chi \right)^{-1}. \quad (7)$$

$\phi_k$  and  $N_k$  are the volume fraction and the degree of polymerization of polymer  $k$ , with  $k = A, B$ .  $\chi$  is the Flory-Huggins interaction parameter. Introducing the reduced temperature

$$\varepsilon = \frac{T - T_c}{T_c}, \quad (8)$$

the critical temperature dependences of  $S(0)$  and the static correlation length  $\xi$  are expressed as scaling laws  $S(0) \sim \varepsilon^{-\gamma}$  and  $\xi \sim \varepsilon^{-\nu}$ . Close to the critical point, in the asymptotic critical region, the scaling exponents take the values  $\gamma = 1.24$  and  $\nu = 0.63$ . The mean field values for larger distances from  $T_c$  are  $\gamma = 1.0$  and  $\nu = 0.5$ . The transition from the classical mean field regime to the asymptotic critical regime is marked by the Ginzburg criterion for the static correlation length,  $\xi \approx R_g N^{1/2}$ , and occurs at  $\varepsilon = Gi$ .  $Gi$  is the Ginzburg number and  $R_g$  the polymer radius of gyration. Following the arguments in Ref. [79], the background diffusion coefficient scales like  $D^b \sim \varepsilon^\gamma = \varepsilon$  and the critical enhancement like  $\Delta D \sim \varepsilon^{\nu(1+z_\eta)} \approx \varepsilon^{0.67}$ , where  $z_\eta = 0.063$  is the critical exponent of the viscosity. Because of the larger

absolute temperature excursions in the mean field regime, the thermal activation of the Onsager coefficient with an activation temperature  $T_a$  additionally needs to be taken into account. Hence, we end up with the following temperature dependence of the diffusion coefficient:

$$D \approx \Delta D \sim \varepsilon^{0.67} \quad \text{for } \varepsilon \ll \text{Gi} \quad (9)$$

$$D \approx D^b \sim \varepsilon \exp(-T_a/T) \quad \text{for } \varepsilon \gg \text{Gi} \quad (10)$$

As discussed in Ref. [79], there is no critical enhancement of the thermal diffusion coefficient  $D_T$ , which retains its background value  $D_T^b$  throughout the asymptotic critical regime. It appears reasonable to assume the same activation temperature  $T_a$  both for  $\alpha^b$  and  $D_T^b$ :

$$D_T = D_T^b = D_T^0 \exp(-T_a/T). \quad (11)$$

Combining Eqs. (9), (10), and Eq. (11), the critical scaling of the Soret coefficient in the asymptotic critical ( $\varepsilon \ll \text{Gi}$ ) and in the mean field regime ( $\varepsilon \gg \text{Gi}$ ) is

$$S_T \approx \frac{D_T^b}{\Delta D} \sim \Delta D^{-1} \sim \varepsilon^{-\nu(1+z_\eta)} \sim \varepsilon^{-0.67} \quad \text{for } \varepsilon \ll \text{Gi} \quad (12)$$

$$S_T \approx \frac{D_T^b}{D^b} = \frac{D_T^b}{\alpha^b/S(0)} \sim S(0) \sim \varepsilon^{-1} \quad \text{for } \varepsilon \gg \text{Gi} \quad (13)$$

Since there had not been any measurements of thermal diffusion and Soret coefficients in polymer blends, the first task was the investigation of the Soret effect in the model polymer blend poly(dimethyl siloxane) (PDMS) and poly(ethyl-methyl siloxane) (PEMS). This polymer system has been chosen both because of its conveniently located lower miscibility gap with a critical temperature that can easily be adjusted within the experimentally interesting range between room temperature and 100 °C by a suitable choice of the molar masses [81, 82]. Furthermore, extensive characterization work has already been done for PDMS/PEMS blends, including the determination of activation energies and Flory-Huggins interaction parameters [7, 8, 83, 84].

## 2.2 The transient grating technique

The transport coefficients have been measured by the transient holographic grating technique of Thermal Diffusion Forced Rayleigh Scattering (TDFRS), that has already been described in more detail in previous works [85, 86, 87] and will only briefly be sketched in the following (Fig. 1).

An argon ion laser operating at 488 nm is split into two beams of equal intensities that are brought to intersection within the sample under an angle  $\theta$  to create a holographic interference grating with a period

$$d = \frac{2\pi}{q} = \frac{\lambda}{2 \sin(\theta/2)}. \quad (14)$$

Energy is absorbed from the light field by an inert dye (quinizarin) that is added to the polymer blend in minute quantities. Neither the phase behavior nor the critical temperature are influenced by the dye. The temperature grating and the secondary concentration grating both couple to the refractive index grating due to the contrast factors  $(\partial n/\partial c)_{p,T}$  and  $(\partial n/\partial T)_{p,c}$ . The resulting phase grating is read by Bragg diffraction of a readout laser beam (HeNe, 633 nm). The diffracted signal beam is mixed with a coherent reference wave derived from a local oscillator in order to create a heterodyne signal for increased sensitivity at low diffraction efficiencies. Electro-optic modulators are used for switching of the phase of the grating and a piezo-mirror serves for phase stabilization. Details of the stabilization and switching procedure and the separation of heterodyne and homodyne signal components have been described in Ref. [88]. A photo multiplier tube operating in photon counting mode is used for detection. It is connected to a counter with a time resolution of  $1 \mu\text{s}$ . For a good signal to noise ratio typically  $10^4$  to  $10^5$  individual exposure cycles are averaged.

Taking the absorbed optical power density as source term  $S = \alpha_\lambda I(\rho c_p)^{-1}$  in the heat equation (5), an analytical expression for the normalized heterodyne diffraction efficiency can be derived as a cascaded linear response [88, 89]:

$$\zeta_{het}(t) = 1 - e^{-t/\tau_{th}} - \frac{\zeta_c}{\tau - \tau_{th}} \left[ \tau \left( 1 - e^{-t/\tau} \right) - \tau_{th} \left( 1 - e^{-t/\tau_{th}} \right) \right], \quad (15)$$

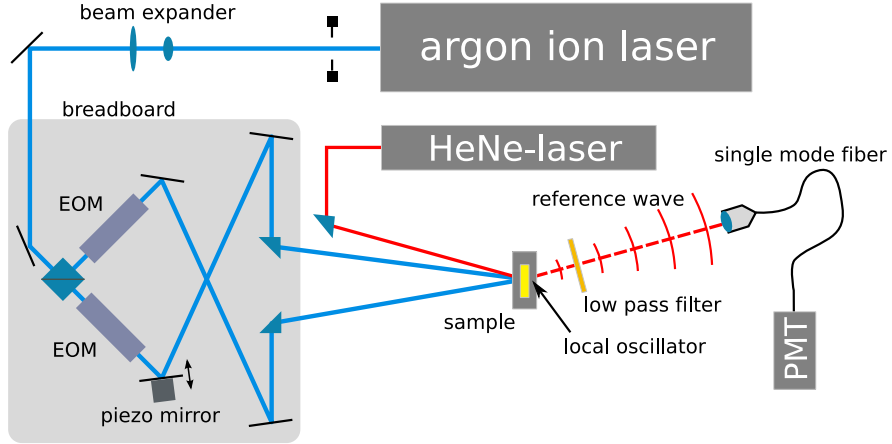


**Fig. 1** The setup for transient holographic grating measurements is shown. The electro-optic modulators (EOMs) are used for  $180^\circ$ -phase shifts of the holographic grating. The piezo mirror serves for phase matching between the diffracted beam and the coherent reference wave generated by the local oscillator. The setup is a modified version of the one described in Ref. [87].

$$\zeta_c = \left( \frac{\partial n}{\partial c} \right)_{p,T} \left( \frac{\partial n}{\partial T} \right)_{p,c}^{-1} S_T c_0 (1 - c_0). \quad (16)$$

$\alpha_\lambda$  is the optical absorption coefficient,  $c_p$  the specific heat, and  $I(x,t) = I_q(t) \exp(iqx)$  the periodic intensity of the light field. The thermal diffusivity and the diffusion coefficient are obtained from the relaxation time constants of the temperature and the concentration grating, which are treated as fit parameters:  $\tau_{th} = (D_{th}q^2)^{-1}$  and  $\tau = (Dq^2)^{-1}$ . The description becomes more complex in case of very thin samples, where heat conduction into the walls becomes important [90].

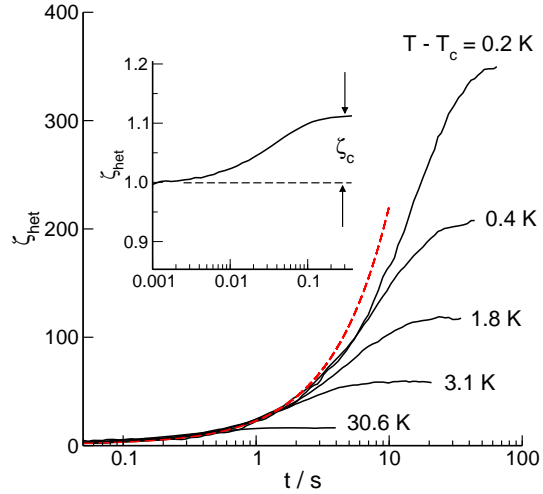
The contrast factors have been measured interferometrically [87] and with an Abbe refractometer, respectively. The sample was contained in a fused silica spectroscopic cell with  $200 \mu\text{m}$  thickness (Hellma). The sample holder is thermostated with a circulating water thermostat and the temperature is measured close to the sample with a Pt100 resistor. The amplitude of the temperature modulation of the grating is well below  $100 \mu\text{K}$  and the overall temperature increase within the sample is limited to approximately  $70 \text{mK}$  in a typical experiment [91], which is sufficiently small to allow for measurements close to the critical point.

### 2.3 Measurements on PDMS/PEMS blends

The measurements near the critical point have been performed with a PDMS/PEMS blend with molar masses of  $M_w = 16.4 \text{kg/mol}$  (PDMS,  $M_w/M_n=1.10$ ) and  $M_w = 22.8 \text{kg/mol}$  (PEMS,  $M_w/M_n=1.11$ ). The corresponding degrees of polymerization are  $N = 219$  and  $N = 257$ , respectively. The phase diagram shows a lower miscibility gap with a critical composition of  $c_c = 0.548$  (weight fractions of PDMS), which was determined according to the equal volume criterion. This value is in good agreement with the critical volume fraction  $\phi_c$  calculated from the Flory-Huggins-model [91]. The critical temperature is  $T_c = 38.6^\circ\text{C}$ . For some measurements also off-critical mixtures of varying molar masses have been employed. The relevant numbers will be given where appropriate.

As predicted by the expressions for the critical divergence of the Soret coefficient in Eq. (12) and Eq. (13), the heterodyne diffraction efficiency of the induced concentration grating dramatically increases on approach of the critical point. Fig. 2 shows normalized heterodyne diffraction efficiencies that have been recorded for different distances  $T - T_c$ . A few hundred milli-Kelvin away from  $T_c$ , the modulation depth, which is proportional to the heterodyne signal, exceeds the values typically found for small molecules and off-critical mixtures already by nearly four orders of magnitude.

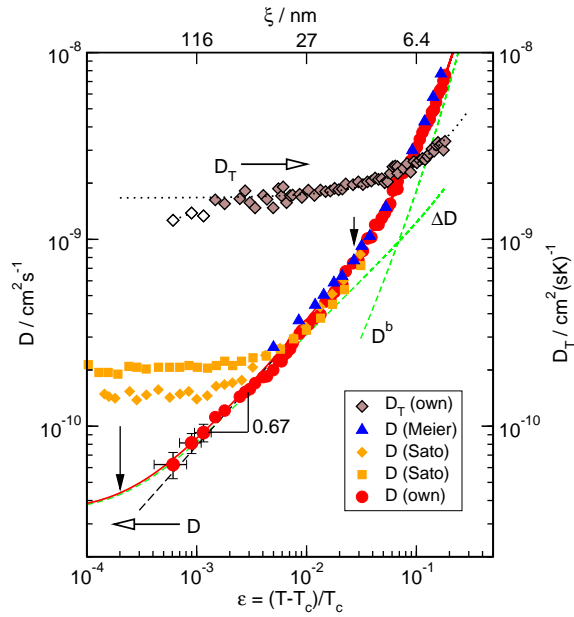
**Fig. 2** Typical heterodyne diffraction signals measured for a critical PDMS/PEMS mixture for different distances  $T - T_c$  to the critical point. All curves have been normalized according to Eq. (15). The dashed line indicates the nearly constant initial slope of the concentration signal (an exponential function in the logarithmic plot) caused by the almost constant value of  $D_T$ . The inset shows, for comparison, a considerably smaller signal for an off critical PDMS/PEMS mixture (860 and 980 g/mol).



## 2.4 The diffusion coefficient

The diffusion coefficient  $D$  is plotted in Fig. 3 as a function of the reduced temperature  $\varepsilon$ . The upper  $x$ -axis shows the correlation length  $\xi = \xi_0 \varepsilon^{-0.63}$  with  $\xi_0 = 1.5$  nm. The short downward arrow marks the approximate locus of the transition from the asymptotic Ising to mean field behavior at  $\xi \approx N^{1/2} R_g$  [4]. Below this value, at

**Fig. 3** Mass and thermal diffusion coefficients  $D$  and  $D_T$  as functions of reduced temperature  $\varepsilon$ . Literature PCS data for  $D$  taken from Meier [8] and Sato [92] (scattering angle  $60^\circ$  ( $\diamond$ ) and  $130^\circ$  ( $\square$ )). See text for a discussion of the fit functions. Also shown  $D_T$  (upper curve, right  $y$ -axis) for the same temperature range together with fit function containing only thermal activation (dotted line). Open diamonds: data with unclear error bars due to very long equilibration times. Note the different units of the two  $y$ -axes.



smaller values of  $\varepsilon$  and larger correlation lengths, the data are compatible with the asymptotic scaling law of Eq. (9). For large values of  $\varepsilon$  the slope continuously increases due to the transition to the mean field exponent and the growing influence of thermal activation [81].

Data of  $D$  as measured previously by photon correlation spectroscopy (PCS) on comparable polymer blends have also been included in Fig. 3. Generally, both the data of Meier [8] and Sato [92] show an excellent agreement with our results. Close to  $T_c$  (below  $\varepsilon \approx 0.01$ ), however, the PCS data level off and no longer follow the asymptotic scaling law. This transition from a diffusive,  $\Gamma = Dq^2 \propto q^2$ , to a non-diffusive behavior with  $\Gamma \propto q^3$ , occurs when the correlation length exceeds the inverse scattering vector,  $\xi > q^{-1}$ . The  $q$ -dependence of the *apparent* diffusion coefficient is evident from the two measurements performed by Sato et al. at different scattering angles.

Since TDFRS works at much lower  $q$ -values than PCS, in our case  $q \approx 3 \times 10^{-3} \text{ nm}^{-1}$  compared to  $q \approx 3 \times 10^{-2} \text{ nm}^{-1}$ , the critical point can be approached much closer on the  $\varepsilon$ -axis, thereby still observing scaling behavior and critical slowing down of  $D$ . The crossover corresponding to  $q^{-1}\xi \approx 1$  is marked with an arrow at  $\varepsilon \approx 2 \times 10^{-4}$ .

An analytical description of the crossover from a diffusive to a non-diffusive behavior at a finite  $q$ -value has been given by Kawasaki [93]:

$$D(q\xi) = D(q \rightarrow 0)K(q\xi), \quad (17)$$

$$K(x) = \frac{3}{4x^2} (1 + x^2 + (x^3 - x^{-1}) \arctan x). \quad (18)$$

A fit of  $D$  taking the Kawasaki function (18) into account is included in Fig. 3 (see next paragraph). It shows the expected significant deviation from the scaling law just outside the  $\varepsilon$ -range of our TDFRS data.

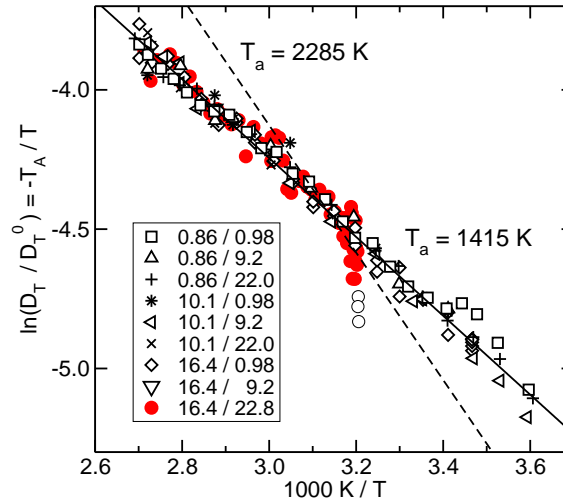
The problem of the dynamic crossover from the Ising to the mean field regime has been treated by Jacob [94] and by Kostko [95]. Kostko et al. derived a decomposition of  $D = D^b + \Delta D$  into a background contribution  $D^b$  and an enhancement  $\Delta D$  of the form

$$D^b = \frac{k_B T (1 + (q\xi)^2)}{6\pi\eta_b\xi} \frac{1}{q_D\xi}, \quad (19)$$

$$\Delta D = \frac{k_B T}{6\pi\eta\xi} K(q\xi) \left[ 1 + \frac{q\xi}{2} \right]^{z_\eta/2} \cdot \frac{2}{\pi} \arctan(q_D\xi). \quad (20)$$

$\eta_b$  is the background contribution of the viscosity and  $q_D^{-1}$  a characteristic cutoff-length.  $K(x)$  is the Kawasaki function defined in Eq. (18). The solid line in Fig. 3, which interpolates our data quite reasonably, is a fit of the sum of Eqs. (19) and (20). The correspondingly labeled dashed lines show the decomposition into the two contributions  $D^b$  and  $\Delta D$ . The viscosity was assumed to be thermally activated with the same activation temperature of  $T_a = 1460 \text{ K}$  as the thermal diffusion coefficient (see below). The weak critical divergence of the viscosity has been neglected. Details

**Fig. 4** Arrhenius plot of the ratio  $D_T/D_T^0$  according to Eq. (11) for critical (16.4/22.8) and a number of off-critical PDMS/PEMS blends of various molar masses and concentrations  $c = 0.5$ . The legends give the PDMS and PEMS molar masses in kg/mol. Also shown is a line corresponding to the activation energy of the viscosity according to Ref. [92]. Fig. according to Ref. [96].

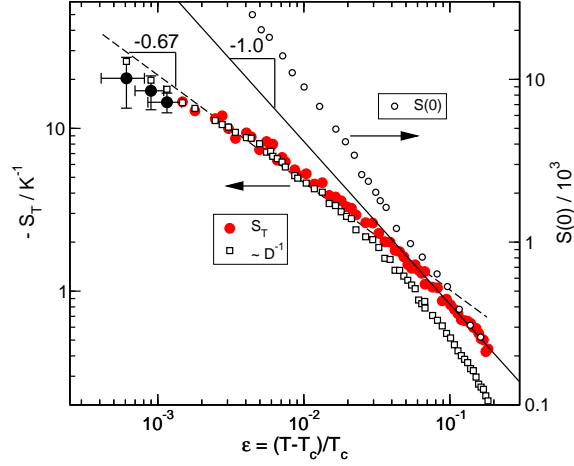


of the analysis and questions associated with the proper choice of the correlation length are discussed in more detail in Ref. [81].

## 2.5 The thermal diffusion coefficient

The data for  $D_T$  in Fig. 3 clearly show, in contrast to the data for  $D$ , no critical scaling but only thermal activation. A fit of the expression in Eq. (11) to the data in Fig. 3 gives a prefactor  $D_T^0 = 1.82 \times 10^{-7} \text{ cm}^2(\text{sK})^{-1}$  and an activation temperature of  $T_a = 1460 \text{ K}$ . Fig. 4 shows an Arrhenius plot of the thermal diffusion coefficient according to Eq. (11) not only for the  $D_T$  data from Fig. 3 but also for a number of off-critical PDMS/PEMS blends of different molar masses and PDMS-concentrations of  $c = 0.5$ . Only the critical mixture has a slightly different concentration of  $c_c = 0.548$ . Independent of the criticality of the system, all activation energies  $k_B T_a$  are identical. A common fit yields an activation temperature of  $T_a = 1415 \text{ K}$ , which is almost identical to the value of  $1460 \text{ K}$  obtained for the critical mixture alone [96]. Also shown in Fig. 4 is a dashed line with the slope corresponding to an activation temperature of  $2285 \text{ K}$  as reported in Ref. [92] for the viscosity. The reason for the pronounced difference between these two activation temperatures is not clear, and a definite answer would require additional viscosity measurements for PDMS/PEMS blends as described in this work. A detailed analysis of  $D_T$  of PDMS/PEMS mixtures of equal weight fractions has shown that the prefactor  $D_T^0$  can be decomposed into a molar mass independent part plus contributions from the end-groups, which vanish for longer chain lengths [96, 97].

**Fig. 5** Soret coefficient  $S_T$  as function of the reduced temperature  $\varepsilon$ . For comparison  $D^{-1}$  with arbitrary multiplicative factor (both left  $y$ -axis) and the static structure factor  $S(0)$  ( $\circ$ ) are shown for a similar blend taken from Ref. [8]. Note the identical dynamical range of both  $y$ -axes. Fig. according to Ref. [81].



## 2.6 The Soret coefficient

According to Eqs. (12) and (13) the Soret coefficient  $S_T = D_T/D$  diverges on approach of the critical point. This scenario is plotted in Fig. 5. Since  $D_T$  is constant to good approximation within this narrow temperature range of only a few Kelvin, the scaling law in the asymptotic critical regime,  $S_T \propto \varepsilon^{-0.67}$ , is determined by the exponent of the diffusion coefficient. At larger  $\varepsilon > Gi$  the Soret coefficient diverges with the mean field exponent of the structure factor  $S(0)$ , since the thermal activation, which appears both in  $D$  and  $D_T$ , cancels out. In order to illustrate this crossover of the divergence of  $S_T$  from the mean field to the asymptotic critical regime, we have included in Fig. 5 besides our own data on  $D^{-1}$  also data from previous works on the static structure factor  $S(0)$  of a comparable PDMS/PEMS (19.4/30.1) blend [8]. The straight line with a slope of -1 has been included in Fig. 5 to demonstrate that the mean field scaling exponent  $\gamma = 1$  can be found for  $S_T$  rather than for  $D$ , which shows a stronger temperature dependence due to the additional thermal activation of the Onsager coefficient  $\alpha^b$ .

Additional insight into the nature of the Soret coefficient and its critical divergence is obtained from Eq. (13) for the classical regime:

$$S_T \approx \frac{D_T}{D^b} = \frac{D_T}{\alpha^b} S(0) = K(T) S(0). \quad (21)$$

Since both  $D_T$  and  $\alpha^b$  are thermally activated with the same activation temperature and with prefactors  $D_T^0$  and  $\alpha^{b,0}$ , the dominating contribution of the temperature dependence cancels out in the ratio and we are left with an only weakly temperature dependent function

$$K(T) = \frac{D_T}{\alpha^b} = \frac{D_T^0}{\alpha^{b,0}}. \quad (22)$$

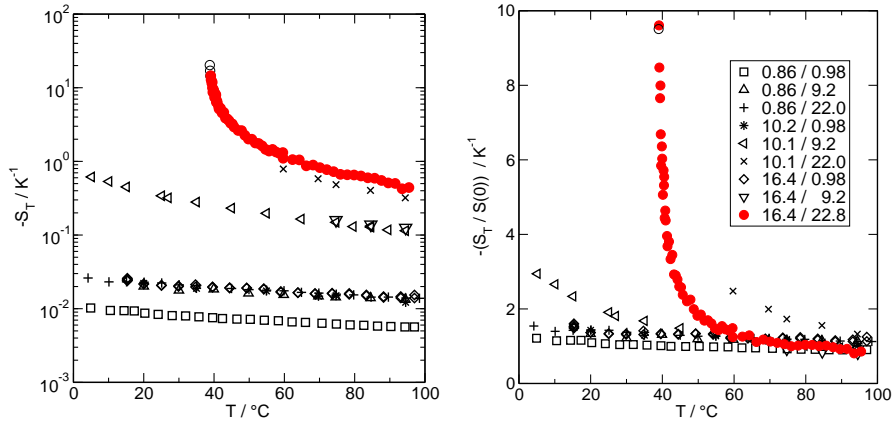


**Fig. 6** Left: Soret coefficient  $S_T$  for a number of PDMS/PEMS blends. The red bullets correspond to the critical blend with a critical temperature of  $T_c = 38.6^\circ\text{C}$ . Right: Same data as left normalized to mean field static structure factor  $S(0)$ . The legends give the PDMS and PEMS molar masses in kg/mol. Figs. according to Ref. [96].

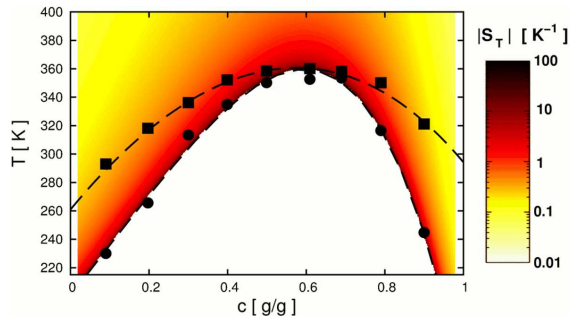
Experiments have shown that, at least for PDMS/PEMS blends of equal weight fraction,  $K(T)$  indeed depends only weakly on temperature and is independent of the molar mass of the constituents [96]. Consequently, the different values of the Soret coefficient in the classical mean field regime are almost exclusively caused by the variation of the static structure factor.

Fig. 6 shows the respective data plotted according to Eq. (21) for a number of blends with different degrees of polymerization. The left plot shows the Soret coefficients as measured and the right one after normalization to the mean field static structure factor calculated from the Flory Huggins model, cf. Eq. (7). Although the structure factors and the Soret coefficients of the different samples vary by more than two orders of magnitude – even at the highest temperature of almost  $100^\circ\text{C}$  – all curves collapse onto one single master curve for a high temperature  $T$ . At lower temperatures there is the pronounced deviation from the common curve for the (16.4/22.8) blend in the asymptotic critical regime with the critical divergence of  $S_T$ . The slight deviations of two other blends might be first hints of phase transitions at lower temperatures [96].

### 3 Laser-thermal patterning of the homogeneous phase

Structuring of polymer films attracts considerable attention, and various radiation sources have been employed to selectively crosslink suitable polymers for e.g. waveguide fabrication [98]. Incompatible polymer blends have been forced into certain demixing morphologies along pre-patterned surfaces [55]. Persistent structures

**Fig. 7** Phase diagram of PDMS/PEMS (16.4/48.1). The cloud points that mark the binodal (squares) have been obtained by turbidimetry. Pseudo-spinodal points as explained in the text. The color encodes the modulus of the Soret coefficient. Fig. from Ref. [99].



could be formed by laser radiation in various non-absorbing polymer solutions, such as polyisoprene in n-hexane [58, 57].

In the following we will describe a novel photothermal patterning technique that relies on the Soret effect. The diverging Soret coefficient in a polymer blend close to the critical point leads to a very strong coupling of the order parameter, the local composition, to an externally prescribed inhomogeneous temperature field. This opens an interesting route to the formation of arbitrary composition patterns within an initially homogeneous polymer film. Since there is no photochemistry involved, the whole process is fully reversible and structures can easily be erased by local or global heating of the sample.

Our goal was, to provide a detailed experimental characterization and numerical modeling of the photothermal structure formation in a critical polymer blend. Since the transport coefficients, and in particular the Soret coefficient, strongly depend on temperature and concentration, the structure formation is a highly nonlinear process that requires a detailed knowledge of all relevant coefficients within a broad parameter range. Since useful data on Soret coefficients for polymer blends were not provided by previous works, we started with measurements of Soret coefficients for our model system PDMS/PEMS within the entire one-phase regime above the binodal [99].

### 3.1 Phase diagram and transport coefficients

To be able to measure also off-critical mixtures down to the binodal within a convenient temperature range, a mixture with a higher critical temperature has been chosen than for the previous investigation of the critical behavior. The system chosen was PDMS ( $M_w = 16.4 \text{ kg/mol}$ ,  $M_w/M_n=1.10$ ) and PEMS ( $M_w = 48.1 \text{ kg/mol}$ ,  $M_w/M_n=1.19$ ). It has a critical composition of  $c_c \approx 0.6$  and a critical temperature of  $T_c \approx 354 \text{ K}$ . The phase diagram of this mixture is shown in Fig. 7. The cloud points (squares in Fig. 7), which separate the homogeneous from the phase separated regime, define the binodal and have been determined by turbidimetry. The spinodal and the color-coded Soret coefficient will be discussed later on.

The diffusion, thermal diffusion, and Soret coefficients for nine different PDMS concentrations from  $c = 0.09$  to  $c = 0.9$  have been measured between the binodal temperature and approximately 368 K. Fig. 8 shows on the left side the diffusion and thermal diffusion coefficients. The temperature dependences of the latter are very well described as thermally activated processes according to Eq. (11) with a common activation temperature  $T_a = 1395$  K, which is very close to the 1460 K obtained for the critical blend in section 2.

Within the pseudo-spinodal concept [100, 11] the diffusion coefficient of an off-critical mixture is still described in a similar way as the diffusion coefficient of the critical mixture. Only the critical temperature is now replaced by the temperature  $T_{sp}$  of the spinodal:

$$D = a_0 \frac{T - T_{sp}}{T} \exp(-T_a/T). \quad (23)$$

In contrast to the critical temperature  $T_c$ , the spinodal temperature  $T_{sp}$  is well below the binodal temperature for off-critical mixtures and can hardly be reached due to prior phase separation. The diffusion coefficients in the upper left part of Fig. 8 have been fitted by Eq. (23) with a fixed activation temperature determined from  $D_T$ . The *binodal points* in Fig. 8 mark the boundary of the homogeneous phase at the binodal. The spinodal temperatures  $T_{sp}$  are obtained as a fit parameter for every concentration and together define the (pseudo)spinodal line plotted in the phase diagram in Fig. 7. The Soret coefficient is obtained from Eqs. (11) and (23) as

$$S_T = \frac{D_T}{D} = \frac{D_T^0}{a_0} \left( \frac{T - T_{sp}}{T} \right)^{-1} \quad (24)$$

and diverges at the spinodal temperature (Fig. 8, right).

Although the asymptotic critical regime with the Ising-like scaling exponents has been neglected in this description, the fit curves in Fig. 8 are a reasonable parameterization for all three coefficients in the one-phase regime. This parameterization then serves as input for the numerical model. A more detailed discussion of the whole procedure can be found in Ref. [99].

### 3.2 Writing patterns into polymer films by local laser heating

The huge Soret coefficient near the critical point can be taken advantage of for the creation of compositional patterns by local heating. Fig. 9 shows a setup that has been used in experiments for writing compositional patterns in polymer blends. It consists of an inverted phase contrast microscope equipped with a CCD camera. A Laser beam ( $\lambda = 515$  nm) can be coupled in via a telecentric lens system and a galvano scanner, which allows for arbitrary computer controlled positioning of the laser focus within the sample. The laser is focused down to  $r_0 = 0.8 \mu\text{m}$  and its power can be adjusted between 0.1 and 100 mW. The sample cell is temperature controlled and mounted on a xyz-stage. The polymer layer of  $L_s = 100 \mu\text{m}$  thickness

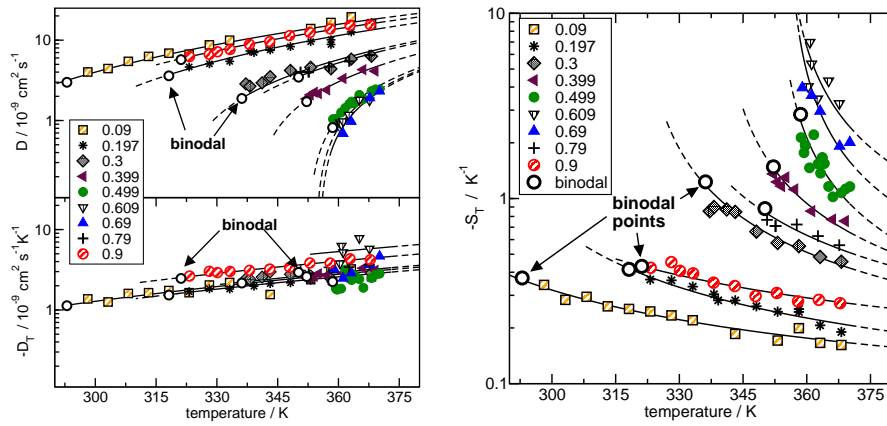


**Fig. 8** Diffusion ( $D$ ) and thermal diffusion ( $D_T$ ) coefficient of PDMS/PEMS (16.4/48.1) (left) and Soret coefficient (right) for different PDMS mass fractions given in the legends. *Binodal points* mark the intersection with the binodal. The dashed line segments are extrapolations into the two-phase regime. Figs. from Ref. [99].

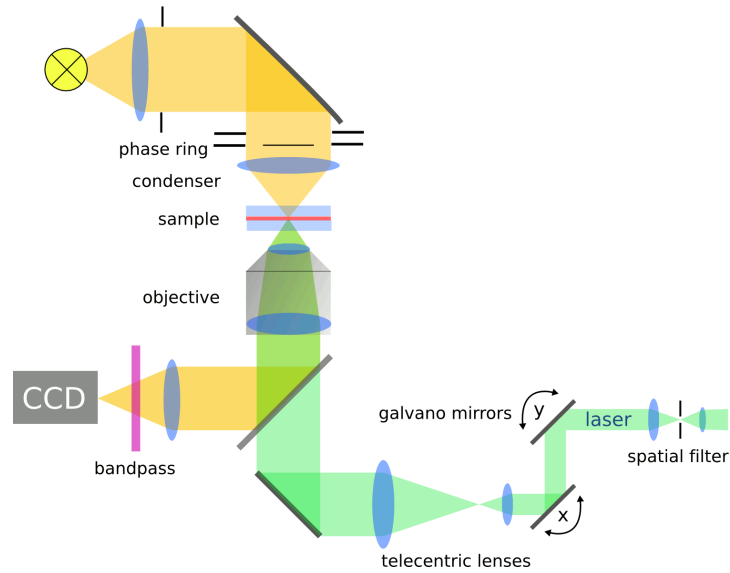


**Fig. 9** Inverted phase contrast microscope equipped with a CCD camera and a laser. Galvano mirrors allow for scanning of the laser focus across the sample.

is sandwiched between two 1 mm thick sapphire windows that are sealed with a two component epoxy resin (Torr Seal). A small amount of dye (quinizarin) is added for optical absorption. It does not change the critical temperature noticeably.

Pattern writing experiments have been performed with an almost symmetric PDMS/PEMS (16.4/15.9) blend having a critical composition  $c_c = 0.48$  and a con-

venient critical temperature  $T_c = 290.15$  K. It has been shown in Ref. [99] in detail that the parameterization of the transport coefficient determined for the higher PEMS molar mass still yields a good description also for this blend after adjusting the critical concentration and taking  $(T - T_{sp})/T$  as dimensionless temperature.

The focused laser beam is scanned along an arbitrary path within the  $xy$ -plane as sketched in Fig. 10. The perspective view with the cross section through the scan path shown in Fig. 10a) visualizes the color-coded concentration change due to the Soret effect according to the numerical simulation discussed later on. On the right hand side a phase contrast micrograph is shown where the word *Soret* has been written into the polymer blend.

For a quantitative analysis a short line segment has been written at two different distances  $\Delta T = 1$  K and  $11.5$  K above  $T_c$ , cf. Fig. 11. Because of the positive phase contrast, a darker gray value translates into a higher refractive index. Hence, the polymer with the lower refractive index (PDMS) is enriched within the bright central region. Consequently, PEMS migrates into the opposite direction and causes a dark fringe around the bright lines. These effect also leads to the darker halos around the letters in Fig. 10. This observation is in agreement with the negative sign of  $S_T$  reported in Fig. 5 for PDMS/PEMS.

The initial linear growth is proportional to  $D_T$  and identical for both distances from  $T_c$ , cf. Fig. 11 A and D. At longer times the line written at  $\Delta T = 11.5$  K quickly saturates, whereas the line written close to  $T_c$  continues to grow in intensity due to the much larger Soret coefficient, as indicated in Fig. 11 C and F.

The gray values in Fig. 10 and in Fig. 11 are two-dimensional projections into the  $xy$ -plane. Because of the phase contrast technique, they are approximately linear functions of the integral over the refractive index along the  $z$ -direction. The temperature and concentration distribution and, hence, also the refractive index are fully three-dimensional objects. The high thermal conductivity of the sapphire windows enforces a constant temperature boundary condition at the top and bottom windows.

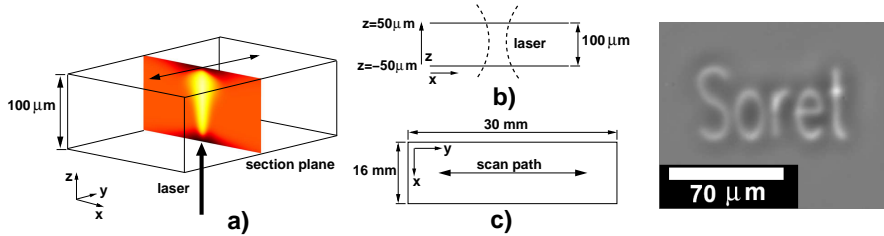


**Fig. 10** a) 3d-sketch of the cell. The laser beam is scanned along the  $y$ -direction (c); cross-section according to Fig. 12. b) Sketch of laser focus. Right: arbitrary pattern written into critical sample.

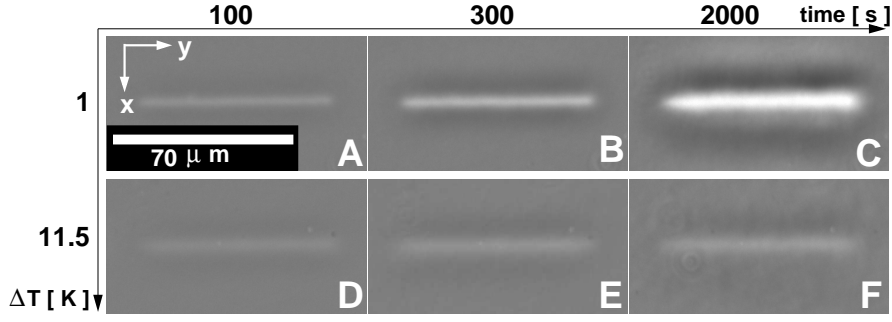


**Fig. 11** Phase contrast micrographs of line segment written 1 K (upper row) and 11.5 K (lower row) above  $T_c$  into PDMS/PEMS blend of critical composition. Images in columns taken after 100, 300, and 2000 seconds. Fig. from Ref. [99].

### 3.2.1 Numerical model

A more detailed picture of the three-dimensional temperature and concentration distribution can be obtained by an appropriate numerical model. Besides the diffusion equations for heat and mass, convection caused by both thermal and solutal expansion needs to be taken into account.

The temperature profile evolves according to the heat equation (Eq. 5) with the heat source supplied by absorption of the focused laser beam. An additional advection term accounts for the influence of convection:

$$\frac{\partial T}{\partial t} + (\mathbf{v} \cdot \nabla) T = \nabla \cdot (D_{th} \nabla T) + \frac{\alpha}{\rho c_p} I. \quad (25)$$

The heating Gaussian laser beam is scanned along the  $y$ -direction. It enters the sample at  $z = -L_s/2$  and creates an intensity distribution

$$I = \frac{P_0}{A} \exp \left[ -\frac{2\{x^2 + (y - s(t))^2\}}{r^2} \right] \exp \left[ -\alpha \left( \frac{L_s}{2} - z \right) \right], \quad (26)$$

$$A = \pi r^2 / 2,$$

$$r^2 = r_0^2 \left[ 1 + \left( \frac{\lambda z}{\pi r_0^2} \right)^2 \right].$$

The temporally periodic scanning of the laser is described by  $s(t)$ , which changes from  $-L_{line}/2$  to  $+L_{line}/2$  linearly in time. For coordinate axes see Fig. 10.

As in case of the heat equation, an advection term must be added to the diffusion equation (3):

$$\frac{\partial c}{\partial t} + (\mathbf{v} \cdot \nabla) c = \nabla \cdot [D \nabla c + D_T c (1 - c) \nabla T]. \quad (27)$$

Convection is accounted for by the Navier-Stokes equation in the Boussinesq approximation

$$\rho_0 \left[ \frac{\partial \mathbf{v}}{\partial t} + (\mathbf{v} \cdot \nabla) \mathbf{v} \right] = -\nabla p + \eta_0 \nabla^2 \mathbf{v} - \rho g \mathbf{e}_z \quad (28)$$

with the incompressibility condition

$$\nabla \cdot \mathbf{v} = 0. \quad (29)$$

The density changes because of both thermal and solutal expansion with expansion coefficients  $\beta_T = -(1/\rho)(\partial\rho/\partial T)_c$  and  $\beta_c = (1/\rho)(\partial\rho/\partial c)_T$ , respectively:

$$\rho = \rho_0 [1 - \beta_T(T - T_0) + \beta_c(c - c_0)]. \quad (30)$$

$\rho_0$  is the mean density at temperature  $T_0$ .

Since the extension of the induced concentration profile in Fig. 11 along the  $y$ -axes is much longer than along the other two directions, we assume translation symmetry and restrict our description to a two-dimensional model within the  $xz$ -plane. The intensity of the laser beam is obtained by averaging Eq. (26) over the scan period:

$$\begin{aligned} I &= (P_0/A) \exp \left[ -\frac{2x^2}{r^2} \right] \exp \left[ -\alpha \left( \frac{L_s}{2} - z \right) \right], \quad (31) \\ A &= \sqrt{\frac{\pi}{2}} \frac{r L_{line}}{\operatorname{erf}(L_{line}/\sqrt{2}r)}, \\ r^2 &= r_0^2 \left[ 1 + \left( \frac{\lambda z}{\pi r_0^2} \right)^2 \right]. \end{aligned}$$

The high thermal conductivity of the sapphire windows ensures a fixed temperature  $T = T_0$  at the boundaries  $z = \pm L_s/2$  and at  $x = \pm L_x/2$ . The boundary condition for the diffusion equation is a vanishing flux at the walls (normal vector  $\mathbf{e}_n$ ):

$$\mathbf{e}_n \cdot [D\nabla c + D_T c(1-c)\nabla T] = 0. \quad (32)$$

For the velocity one has a non slip boundary condition at the walls:  $\mathbf{v} = 0$ . The initial conditions are  $T = T_0$ ,  $c = c_0$ , and  $\mathbf{v} = 0$ .

An expression for the transmitted light in ideal phase contrast imaging can be found in Refs. [101, 102]. For a more detailed treatment it is also necessary to take the finite width of the phase object into account [103], resulting in

$$\begin{aligned} \frac{I_{Tr} - I_{Tr0}}{I_{Tr0}} &= K \left[ \frac{1 + p^2 + t^2 - 2p(\cos \phi + t \sin \phi)}{1 + p^2 + t^2 - 2p} - 1 \right], \\ \phi &= \frac{2\pi L_s}{\lambda_{hal}} \frac{\partial n}{\partial c} (\bar{c} - c_0). \quad (33) \end{aligned}$$

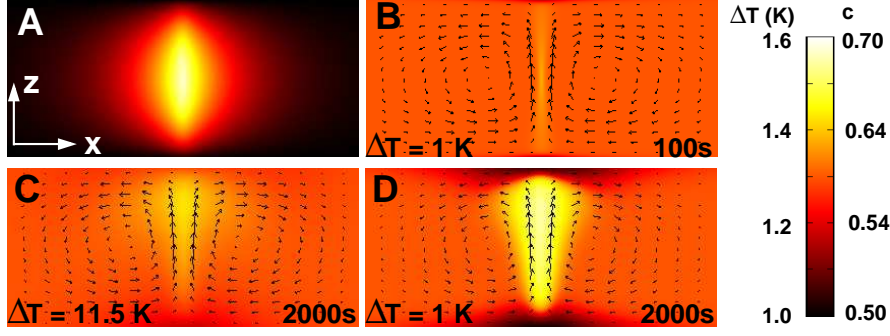


**Fig. 12** Vertical cuts (perpendicular to  $y$ -axis) through a linear structure written by the laser. (A) temperature profile. (B, D) concentration profiles  $c(x,z)$  for a starting temperature of  $\Delta T = 1$  K above the critical temperature after 100 s and 2000 s. Part (C) visualizes like in Part (D) the temperature and concentration for  $\Delta T = 11.5$  K. The arrows are for visualization of the flow fields. Fig. from Ref. [99].

$p^2 = 1$  and  $t^2 = 0.4$  are the relative amplitude transmittance of the polymer layer and the microscope objective, respectively.  $\phi = \phi(x)$  is the phase shift induced in the layer due to the concentration change,  $\lambda_{\text{hal}} = 550$  nm is the wavelength of probing light,  $\partial n/\partial c = -2.3 \times 10^{-2}$  is the contrast factor of the PDMS/PEMS mixture, and  $\bar{c}$  is the concentration averaged over the layer thickness.  $K$  is treated as a fit parameter [99]. The material parameters like viscosity, density, and expansion coefficients are given in Ref. [99].

Fig. 12 shows the result of the numerical solution of the model above. The images are cross sections through a written line perpendicular to the scan direction of the laser. The vertical dimension, the  $z$ -direction, corresponds to a sample thickness of  $100 \mu\text{m}$ . The stationary temperature distribution shown in Fig. 12A is reached very rapidly. Fig. 12B shows the concentration profile after 100 seconds. This image is shown for a distance of  $\Delta T = 1$  K above the critical temperature. The early-stage concentration profile does, however, not depend significantly on the absolute temperature because of the almost constant thermal diffusion coefficient. During the initial linear growth period the concentration profile remains very sharp and resembles the profile of the focused Gaussian laser beam. This seems surprising at a first sight, since the driving temperature profile is already rather broad. It is, however, understood from Eq. (27), which takes for short times the form

$$\frac{\partial c}{\partial t} \Big|_{t \rightarrow 0} = D_T c(1-c) \nabla^2 T. \quad (34)$$

Hence, the early stage of the concentration profile is proportional to the Laplacian of  $T(\mathbf{r}, t)$  rather than the temperature field itself. From the stationary solution of Eq. (25) it can be seen that  $\nabla^2 T(\mathbf{r}, t)$  is proportional to the laser intensity, neglecting temperature dependences of the coefficients and convection in a first approach.

At longer times the concentration profile broadens and becomes more intense. The two images at  $t = 2000$  s clearly show the much stronger effect close to the

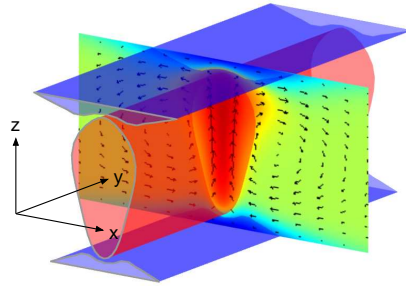
critical point, cf. Fig. 12D. Convection causes an asymmetry of the profile and a detailed analysis shows, that the main effect of convection is the solutal rather than the thermal expansion of the mixture. Radiation pressure effects due to the laser entering from below are approximately one order of magnitude smaller and negligible.

Due to the optical volume heating and the high thermal conductivity of the sapphire, the strongest temperature gradient develops directly at the window surface. Consequently, PEMS enriches mainly at the windows above and below the heated channel rather than to the left and right, as one might first guess from the two-dimensional projection with the dark halos of Fig. 11. PEMS-rich regions appear darker in Fig. 12.

The color-coding of the hot/cold colormap used in Fig. 12 for the concentration profile can also be interpreted in terms of a refractive index map. The refractive indices of the PDMS/PEMS mixtures are such that the bright channel in the center, which corresponds to a PDMS enrichment, has a lower refractive index and the PEMS-rich layers at the windows have a higher refractive index than the average mixture. However, there may exist other polymer blends where the sign change of the refractive index is in the opposite direction. In this case, the channel-like structures could be used as re-writable optical waveguides. The cladding layers, which automatically form at the windows, would then be of low refractive index and shield the channel from the high refractive index of the window material. Such a structure is sketched in a perspective view in Fig. 13. Written structures are fully reversible and can locally or globally be erased by heating. Long term stability might be achievable with blends of a polymer with a low and a high glass transition temperature, where the dynamics comes to rest during the demixing process [105]. As has been shown for concentrated polymer solutions, the Soret coefficient is not influenced by the increasing viscosity in the vicinity of a glass transition [106, 107, 108, 109].

As a direct consequence of the strong temperature and composition dependence of the Soret coefficient near the critical point,  $S_T$  (and  $D$ ) become position dependent within the polymer layer. When the initially homogeneous sample of critical composition is kept slightly above  $T_c$ , the very high value of  $S_T$  leads to strong concentration changes even for small temperature gradients. When a volume element

**Fig. 13** Perspective view of the channel-like structure of Fig. 12D. A different color coding has been chosen for a better discrimination of the various regions. The PDMS-rich channel in the center (red) is sandwiched between two PEMS-rich layers (blue). Fig. from Ref. [104].



is moved away from the critical point in the phase diagram,  $S_T$  decreases and the further excursion along the composition axis is efficiently limited.

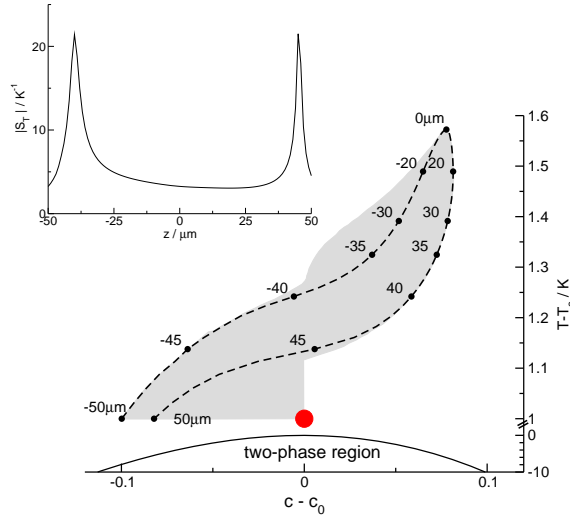
In order to illustrate this nonlinear mechanism we have plotted the part of the phase diagram occupied by the sample from Fig. 12D in Fig. 14 as a gray region. The red bullet marks the initial position of the homogeneous sample just above the critical point. The dashed curve is a trajectory that corresponds to a vertical cut through the cell along the optical axis of the laser beam. Negative values of  $(c - c_0)$  correspond to PEMS, positive values to PDMS enrichment. The Soret coefficient plotted along this trajectory shows a characteristic double peak structure. The two maxima are very close to the position where the concentration crosses the average value  $c = c_0$ .

Fig. 15 shows an example, where the temperature profile has not been created by direct laser heating of the absorbing dyed polymer blend in the volume but rather by optical heating of a colloidal gold particle of 200 nm in diameter [110]. Such a colloid then serves as a microscopic heat source that directly modifies the composition of the surrounding polymer blend. The bright region around the colloid, corresponding to PDMS enrichment, is surrounded by a faint darker ring where PEMS, that is displaced from the immediate surrounding of the gold particle, accumulates.

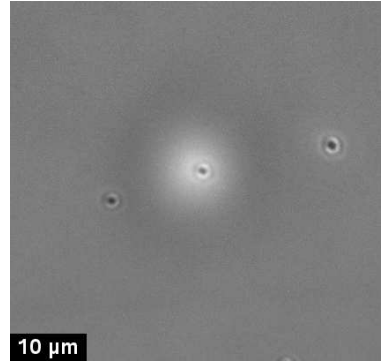
### 3.3 Quenching of an off-critical blend by local heating

Important consequences of the strong coupling between inhomogeneous temperature fields and local composition arise for situations where equilibrium phase diagrams are applied to nonequilibrium systems [111]. Such scenarios have been re-

**Fig. 14** Trajectory in the phase diagram for a vertical cut through the sample corresponding to Fig. 12D.  $z = -50 \mu\text{m}$  and  $z = 50 \mu\text{m}$  correspond to the lower and upper window, respectively. All volume elements of the sample reside inside the gray region. The insert shows the modulus of the Soret coefficient plotted along the dashed trajectory.



**Fig. 15** Phase contrast micrograph of laser-heated gold colloid (center) with PDMS enrichment in the surrounding volume (bright) and PEMS accumulation at larger distance (dark). Only the middle one of the three colloids is heated with a focused laser [110].



ported by a number of authors. Lee et al. studied spinodal decomposition in the presence of a temperature gradient [16, 17]. Tanaka et al. investigated the influence of periodically driving the polymer mixture above and below the instability point [74]. Meredith et al. employed a combinatorial method with perpendicular temperature and concentration gradients in order to determine entire polymer phase diagrams in a single experiment [112]. In the following it will be shown that rather unexpected effects can occur in the presence of temperature gradients and that equilibrium phase diagrams do not necessarily give a valid approach to nonequilibrium conditions.

The experiments reported here have been performed with a PDMS/PEMS (16.4/48.1) blend. The mixture is an UCST mixture with a critical composition of  $c_c = 0.61$ . The diffusion, thermal diffusion and Soret coefficients of this system are shown in Fig. 8. Samples of two different off-critical compositions ( $c = 0.3$  and  $c = 0.9$ ) were prepared. The temperature was set to a value of a few degrees above the binodal. Hence, the sample was entirely within the homogeneous phase

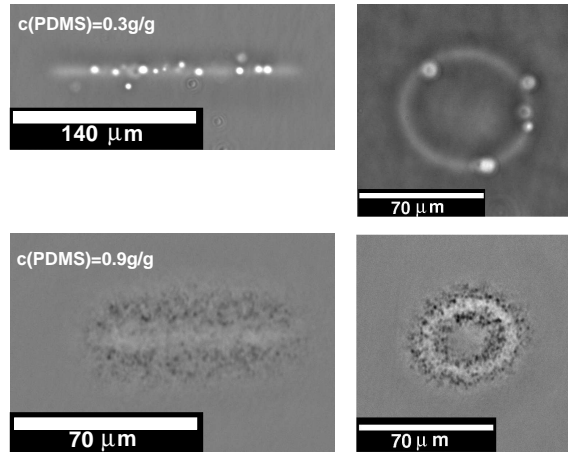
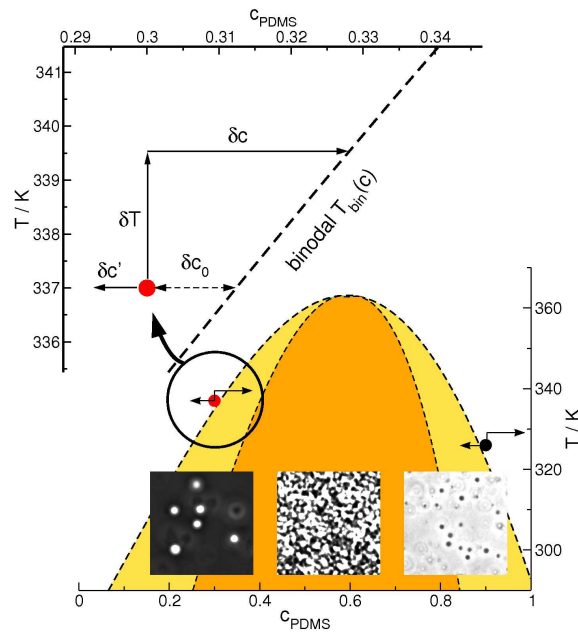


**Fig. 16** Forced demixing of an initially homogeneous off-critical PDMS/PEMS blend for  $c = 0.3$  (upper row) and  $c = 0.9$  (lower row).

**Fig. 17** Phase diagram of a PDMS/PEMS (16.4/48.1) blend. The dashed lines are the binodal and the spinodal. The phase contrast micrographs show typical demixing patterns for spinodal decomposition and nucleation and growth in the respective regions. The bullets mark the initial sample positions. See text for details. Fig. from Ref. [111].



and one would expect that heating could only drive the blend further into the stable one-phase region.

This assumption is indeed true for equilibrium scenarios with a homogeneous temperature distribution. Due to the coupling between heat and mass transport, laser heating gives rise to completely different behavior and can even drive a UCST-mixture locally from the homogeneous into the phase separated state.

The result of such laser writing experiments is shown in Fig. 16, where the focused laser beam has been scanned along simple paths, a line and a circle. The upper two images correspond to the sample with  $c = 0.3$  (left of the binodal), the lower two to  $c = 0.9$  (right of the binodal). The initial location of either sample in the phase diagram is marked in Fig. 17 with bullets. All four images in Fig. 16 show two distinct features. First, there is smooth variation of the gray values with lighter values along the scan path. This reflects the writing with a concentration change due to the Soret effect, similar to the scenario discussed for the critical sample. Additionally, there are localized droplets, which are characteristic for a nucleation and growth type demixing scenario. These droplets are bright and appear in the center of the written line, corresponding to the hottest region, for  $c = 0.3$ . For  $c = 0.9$  they are darker than the average gray value and located at the periphery of the line. In either case their number increases with exposure time.

The occurrence of demixing morphologies characteristic for the metastable regime between the binodal and the spinodal can be understood from Fig. 17. The red dot marks the initial position of the sample with  $c = 0.3$ . Upon laser heating the temperature within the laser focus rises by  $\delta T$  and the distance to the binodal first

increases. A stationary temperature distribution is rapidly reached and the Laplacian of the temperature field  $T(\mathbf{r}, t)$  is obtained from the stationary solution of the heat equation (5) with the power absorbed from the laser as source term:

$$\nabla^2 T = -\frac{\alpha}{\kappa} I \quad (35)$$

Inserting this into the diffusion equation (3) gives an expression for the initial linear growth rate of the concentration profile, where  $\nabla^2 c \approx 0$ :

$$\frac{\partial c}{\partial t} = -\frac{\alpha}{\kappa} D_T c(1-c) I \quad (36)$$

Due to the negative Soret coefficient of PDMS/PEMS, the composition in the center of the focus evolves towards higher PDMS concentrations and, hence, towards the two phase region. The mixture crosses the binodal after a time

$$\delta t = \frac{\delta c}{\partial_t c} = -\frac{\delta c_0 + \delta T (dT_{bin}/dc)^{-1}}{D_T c(1-c) I \alpha / \kappa} \quad (37)$$

$\delta c_0$  is the initial distance to the binodal as defined in Fig. 17.  $(dT_{bin}/dc)$  is the slope of the binodal.  $\delta T = 2.5\text{K}$  has been obtained from a full 3d-simulation of the thermal part of the problem. Details of this estimation, including estimations for all missing parameters, are discussed in Ref. [111]. The estimated time  $\delta t \approx 13\text{s}$  turned out to be much shorter than the seven minutes until first droplets could be observed. Possibly, the much longer waiting time is owed to the metastability of the region between the binodal and the spinodal.

The arrow pointing from the initial location at  $c = 0.3$  to the left indicates the evolution of the concentration away from the center of the heated line and at the window surfaces, corresponding to the blue cladding layers in Fig. 12. These regions represent the cold side with a reduced PDMS and increased PEMS concentration that are shifted further into the stable region, away from the phase boundary.

The situation is different for  $c = 0.9$ , where the PDMS-enriched central part is stabilized and shifted away from the binodal. But now, the regions outside the central area, where PEMS accumulates, cross the phase boundary into the metastable range. The demixing by nucleation and growth is visible in the lower two micrographs in Fig. 16 in form of a halo of dark droplets around the written structures.

Due to the phase contrast technique, PDMS- and PEMS-rich areas can easily be distinguished, as shown in the three micrographs inserted in Fig. 17. They show characteristic demixing scenarios observed for samples homogeneously quenched into the two-phase region. The image in the middle corresponds to a symmetric spinodal demixing pattern. The image on the left side shows droplet formation characteristic for the metastable region to the critical concentration, where PDMS-rich droplets form the minority phase. They appear as bright spots with a dark background. Clearly, the forced demixing of the samples with  $c = 0.3$  in Fig. 16 corresponds to this scenario.

For samples with high PDMS concentrations  $c > c_c$  the situation is the other way around. The droplets of the PEMS-rich minority phase appear dark in front of a bright background. The right micrograph in Fig. 17 and the samples with  $c = 0.9$  in Fig. 16 correspond to this situation.

As a consequence of these experiments one has to realize that care is required in situations where equilibrium phase diagrams are applied to nonequilibrium situations [112]. Due to the coupling of heat and mass transport, the local concentration may change. An excursion along the temperature axis unavoidably leads to a simultaneous excursion along the concentration axis. Due to the large Lewis number, these two effects are characterized by very different characteristic relaxation times.

#### 4 Model for phase separation including thermodiffusion

A modified Cahn-Hilliard (CH) model [113] is used for the theoretical analysis of the impact of thermal diffusion on phase separation, by taking into account an inhomogeneous temperature distribution which couples to a concentration variation via the Soret effect. We use the Flory-Huggins model for the free energy of binary polymer-mixtures. The composition is naturally measured in terms of volume fraction  $\phi$  of a component  $A$ , which can be related to the weight fraction  $c$  by

$$c = \frac{\phi \rho_A}{\phi \rho_A + (1 - \phi) \rho_B}, \quad (38)$$

where  $\rho_A$  and  $\rho_B$  are the densities of the two polymers. For all polymer blends considered in this study, the densities of the two components are assumed to be similar and, therefore, volume and weight fractions can be considered to be identical for all practical purposes. For an incompressible binary  $A/B$  mixture ( $\rho = \text{const}$ ) the continuity equation relates the spatial and time dependence of the local volume fraction  $\phi(\mathbf{r}, t)$  to the total mass current  $\mathbf{J}(\mathbf{r}, t)$ , and expresses the conservation of mass in the system

$$\frac{\partial \phi(\mathbf{r}, t)}{\partial t} = -\nabla \cdot \frac{\mathbf{J}(\mathbf{r}, t)}{\rho}, \quad \mathbf{J} = \mathbf{J}_D + \mathbf{J}_T. \quad (39)$$

Here  $\mathbf{J}_D$  is the mass current related to gradients of the chemical potential  $\mu (= \mu_A - \mu_B)$ , and  $\mathbf{J}_T$  is the mass current due to the Soret effect in a inhomogeneous temperature field  $T$  [76]

$$\mathbf{J}_D(\mathbf{r}, t) = -\rho M (\nabla \mu)_T, \quad \mathbf{J}_T(\mathbf{r}, t) = -\rho D_T \phi (1 - \phi) \nabla T(\mathbf{r}, t), \quad (40)$$

where  $M$  is the ‘‘mobility’’ of species  $A$  with respect to  $B$ , and  $D_T$  is the thermal diffusion coefficient. Both are often treated as a constant although they are concentration dependent in general.

In a Ginzburg-Landau model the chemical potential  $\mu$  is related to the free energy functional  $F[\phi(\mathbf{r}, t)]$  via the expression

$$\mu = \frac{\delta F[\phi]}{\delta \phi}, \quad \frac{F[\phi]}{k_B T} = \frac{1}{v} \int d\mathbf{r} \left[ \frac{f[\phi]}{k_B T} + \kappa(\phi)(\nabla \phi)^2 \right], \quad (41)$$

with the Boltzmann constant  $k_B$ . The Flory-Huggins (FH) expression for the mixing energy of an incompressible binary polymer blend has the following form [80]

$$\frac{f[\phi]}{k_B T} = \frac{\phi}{N_A} \ln \phi + \frac{(1-\phi)}{N_B} \ln(1-\phi) + \chi \phi(1-\phi), \quad (42)$$

where  $N_A$  and  $N_B$  describe the degree of polymerization (“chain lengths”) of the  $A$  and  $B$  sort of molecules, respectively.  $\chi$  is the Flory interaction parameter that describes the interaction strength between the two species  $A$  and  $B$  and positive values of  $\chi$  favor phase separation. This contribution to the free energy has a double-well structure in the two-phase region and the temperature dependence of the coefficient  $\chi$  is commonly described by the following phenomenological expression,

$$\chi = \alpha + \beta T^{-1}, \quad (43)$$

with two empirical constants,  $\alpha$  and  $\beta$  [114].

For positive values of  $\kappa(\phi)$  the gradient term in Eq. (41) expresses the energy required to create an interface between  $A$ -rich and  $B$ -rich domains and this energy contribution is reduced by removing interfaces during the coarsening process in the two phase region. For the coefficient of the gradient term in Eq. (41) we use the de Gennes’ random phase approximation

$$\kappa(\phi) = \frac{1}{36} \left[ \frac{\sigma_A^2}{\phi} + \frac{\sigma_B^2}{1-\phi} \right], \quad (44)$$

where  $\sigma_A$  and  $\sigma_B$  are the monomer sizes (Kuhn lengths) of the  $A$  and  $B$  components, respectively.

Since we have in mind polymer blends subjected to an inhomogeneous temperature field (produced, e.g., by light absorption), the heat equation

$$\frac{\partial T(\mathbf{r}, t)}{\partial t} = D_{th} \nabla^2 T(\mathbf{r}, t) + \frac{\alpha_\lambda}{\rho c_p} I(\mathbf{r}, t) \quad (45)$$

has to be taken into account, where  $D_{th}$  is the thermal diffusivity. The heat source term is proportional to the light intensity  $I$  that corresponds to the local illumination of the polymer film. Here  $\alpha_\lambda$  is the optical absorption coefficient,  $\rho$  is the density, and  $c_p$  the specific heat at constant pressure. For typical polymer blends the Lewis number, describing the ratio between the temperature diffusion time and the mass diffusion time, is of the order of  $10^{-3}$ . Therefore, one can treat the heat equation (45) in the stationary limit (neglect the time derivative of the temperature).

A mixture of composition  $\phi_0$  is unstable against phase separation when  $f[\phi]$  has negative curvature at  $\phi = \phi_0$ . The critical point of spinodal decomposition in model (42) is given by

$$\phi_c = N_B^{1/2}/(N_A^{1/2} + N_B^{1/2}), \quad \chi_c = [N_A^{1/2} + N_B^{1/2}]^2/(2N_A N_B), \quad (46)$$

such that the system is miscible for  $\chi < \chi_c$  and immiscible for  $\chi > \chi_c$  at the critical concentration. Close to  $(\phi_c, \chi_c)$  the expression for the free energy in (42) can be approximated by a Taylor expansion with respect to the composition fluctuation  $\varphi(\mathbf{r}, t) = [\phi(\mathbf{r}, t) - \phi_c]$  leading to the Ginzburg-Landau functional in terms of powers of  $\varphi$  (an irrelevant term linear in  $\varphi$  has been omitted)

$$\frac{F_{GL}[\varphi]}{k_B T_c} = \frac{1}{v} \int d\mathbf{r} \left[ \frac{1}{2} b \varphi^2 + \frac{1}{4} u \varphi^4 + \frac{1}{2} K (\nabla \varphi)^2 \right], \quad (47)$$

where the coefficients are defined as

$$b = 2(\chi_c - \chi) \approx \frac{2\beta}{T_c^2} (T - T_c), \quad u = \frac{4}{3} \chi_c^2 \sqrt{N_A N_B},$$

$$K = \frac{1}{18} [\sigma_A^2 (1 + \sqrt{N_A/N_B}) + \sigma_B^2 (1 + \sqrt{N_B/N_A})]. \quad (48)$$

Eq. (39) and Eq. (45) in combination with Eq. (40) and Eq. (47) define our model close to the critical point:

$$\partial_t \varphi(\mathbf{r}, t) = \frac{M k_B T_c}{v} \nabla^2 [b(T) \varphi + u \varphi^3 - K \nabla^2 \varphi] + D_T \phi_c (1 - \phi_c) \nabla^2 T, \quad (49)$$

$$D_{th} \nabla^2 T = - \frac{\alpha_\lambda}{\rho c_p} I(\mathbf{r}, t). \quad (50)$$

$S_T = D_T/D$  is the Soret coefficient with the diffusion coefficient  $D = (M k_B T_c |b|)/v$ . In the absence of thermal diffusion, Eq. (49) reduces to the well known Cahn-Hilliard equation, which is also known as model *B* [3]). In fact, Eq. (49) gives a universal description of a system in the vicinity of a critical point leading to spinodal decomposition.

## 5 Temperature modulations in the two-phase regime

We will demonstrate in this section how spinodal decomposition pattern in the two phase region can be locally manipulated in a controlled way by heating a polymer blend PDMS/PEMS by a focused laser beam. It is also shown, that the essential spatial and temporal phenomena, as observed in the experiments, can only be reproduced in numerical simulations when thermodiffusion (Soret effect) is taken into account in the basic equations.

The polymer blend PDMS/PEMS with molar masses of  $M_w = 16.4$  and  $22.3$  kg/mol, respectively, was similar to the one which has previously been used for the investigation of transport properties in the critical regime [81] and a laser with  $515$  nm and  $20$  mW has been used for local heating. The blend of with a PDMS weight fraction of  $c = 0.536$  was almost critical with a critical temperature of  $T_c = 37.7$  °C. A minute amount of an inert dye (quinizarin) was added for optical absorption at wavelength of the laser. The thickness of the sample was  $200$   $\mu\text{m}$ , the beam waist approximately  $30$   $\mu\text{m}$ , the optical density  $0.1$  and the temperature rise within the beam center was estimated to be approximately  $5$  K. Images of the sample were recorded by a microscope objective ( $7\times$ ) and a CCD camera, whose image sensor was, without additional optical elements, within the image plane  $50$  cm behind the objective. The horizontally oriented sample was illuminated with slightly divergent white light from a cold light source, which produces an observable amplitude image from a pure phase object. This method of imaging of spinodal decomposition patterns in mixtures of non-absorbing liquids of different refractive indices has been discussed in detail in Ref. [115].

The sample was quenched into the two-phase region  $0.5$  °C below  $T_c$  and  $120$  min later, where also Fig. 18(A) was taken, the laser beam was turned on at  $t = 0$ . At this moment the spinodal decomposition has already reached a progressed stage, and the Fourier transform of Fig. 18(A) gives a characteristic length scale of the order of  $10$   $\mu\text{m}$ . At the time  $t = 200$  sec the laser beam has been turned off and Fig. 18(B) was taken at  $t = 300$  sec. Since the spatial concentration distribution of the two polymers cannot be extracted quantitatively by direct imaging techniques, the gray scales of the experimental images in Fig. 18 have been equalized for optimum contrast.

The spinodal pattern completely disappears in the area, where the material was heated by the laser beam beyond  $T_c$ . After the laser is switched off, this circular pattern again survives for a long time [Figs. 18(B),(C)], before in this area a somewhat irregular structure develops, which slowly grows in diameter [Fig. 18(C)] and moves away from the central spot like a spherical wave.

To analyze this phenomenon further, two-dimensional numerical simulations of Eq. (49) and Eq. (50) were performed using a central finite difference approximation of the spatial derivatives and a 4-th order Runge-Kutta integration of the resulting ordinary differential equations in time. Details of the simulation technique can be found in Ref. [113, 116]. The material parameters of the polymer blend PDMS/PEMS were used and the spatial scale  $\xi = (K/|b|)^{1/2}$  and time scale  $\tau = \xi^2/D$  were established from the experimental measurements of the structure factor evolution under a homogeneous temperature quench.

The results of the simulations, including the Soret-effect, are shown in Fig. 18(a)-(c) for parameters comparable to the experimental conditions. The dark and bright areas correspond according to the basic equations to the A- and B-rich phase, whereas the experimental images are generated by an optical imaging technique, from which only characteristic patterns and length scales are directly comparable. For comparison simulations were also performed without the Soret effect, cf. Fig. 18( $\alpha$ )-( $\gamma$ ), by setting  $D_T = 0$  in Eq. (49). All other parameters of the model were kept constant and the same initial conditions were used in Fig. 18(a) and

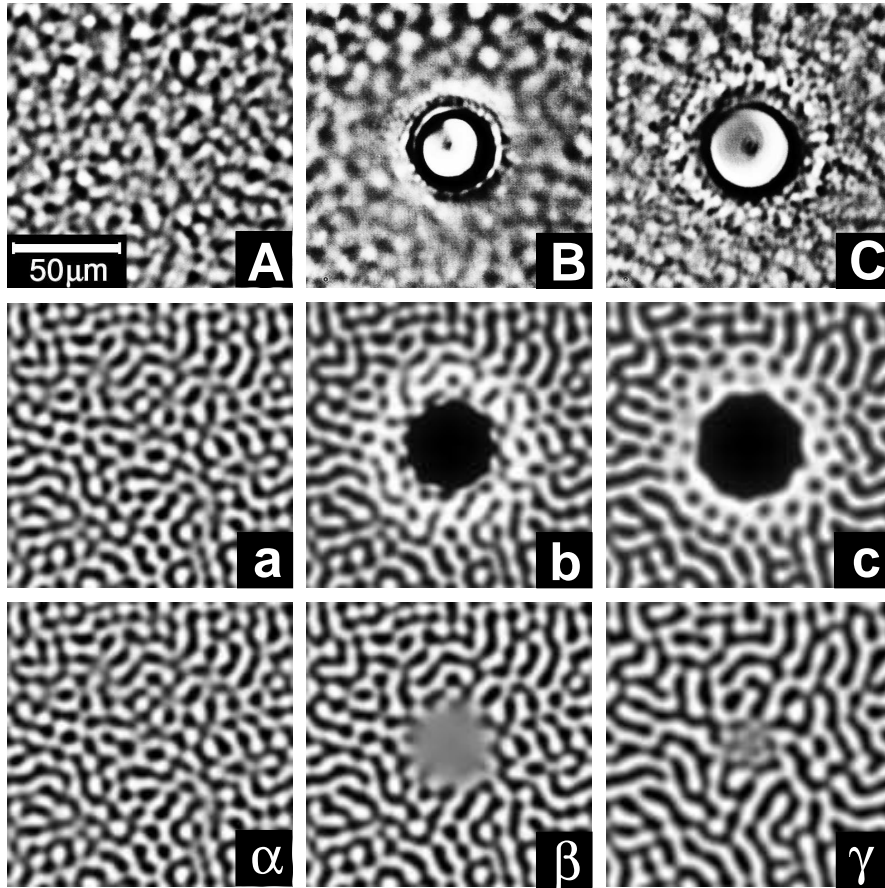


**Fig. 18** Temporal development of a pattern in a polymer blend at  $T = 37.2 \text{ }^\circ\text{C} < T_c$  which was exposed locally to laser light during the period  $0 < t < 200 \text{ s}$ . Images are taken at  $t = 0$  (A),  $t = 300 \text{ s}$  (B), and  $t = 700 \text{ s}$  (C). The corresponding images (a-c) are obtained by simulations with and the images ( $\alpha - \gamma$ ) without taking the Soret effect into account. Fig. from Ref. [116].

Fig. 18( $\alpha$ ). In this case the laser heated spot is driven into the one-phase regime during the laser light exposure, but the characteristic features of the experimentally observed demixing pattern do not show up without the Soret effect.

Our simulations clearly demonstrate that without thermally driven mass diffusion the spatial variation of the control parameter  $b(T)$  due to the local laser heating does not provide the typical pattern evolution observed in the experiments. It is crucial to take the Soret effect in the basic equations into account in order to reproduce the experimentally phenomena observed by local heating.

We have demonstrated that in the two-phase region the spinodal demixing pattern can locally be manipulated on a mesoscopic length scale by local heating. We expect the smallest achievable structures to be in the region of the diffraction limit of the

laser beam. These new effects are not limited to the cylindrical geometries discussed here and may possibly open a new route towards the structuring of polymer blends and towards the creation of gradient materials and embedded gradient structures.

## 6 Spatially periodic forcing of phase separation

A number of interesting effects occur in spatially periodically forced pattern forming systems with a non-conserved order parameter, which have been investigated during the recent years [60, 61, 62, 63, 64, 65, 66, 67, 117, 68, 69, 70, 71, 72, 73]. Here we focus on nearly unexplored effects of spatially periodic forcing in system with a conserved order parameter, as they occur in phase separating systems which are forced by spatial temperature modulations and where thermodiffusion plays a crucial role.

Such forced phase separating systems can be realized, for instance, in optical grating experiments on polymer blends with a spatially periodic light intensity  $I(\mathbf{r}, t) = I_0 \cos(qx)$  [44, 87]. A spatially periodic light intensity leads with Eq. (50), to the following equation

$$\nabla^2 T = -\delta T_0 q^2 \cos(qx), \quad \delta T_0 = \frac{\alpha_\lambda}{\rho c_p D_{th}} \frac{I_0}{q^2}, \quad (51)$$

which determines the spatially periodic temperature field. The contribution  $\nabla^2 T$  in Eq. (49) can be replaced with this equation and one obtains an additive spatially periodic forcing contribution in Eq. (49). On this route we introduce dimensionless variables by choosing the temperature  $T_0$  in the two-phase region as our reference temperature ( $T_0 < T_c$ ) and we write

$$\mathbf{r} = \mathbf{r}' \xi, \quad \xi = (K/|b|)^{1/2}; \quad t = t' \tau, \quad \tau = \xi^2/D; \quad \varphi = \psi(u/|b|)^{-1/2}, \quad (52)$$

where all quantities are evaluated at  $T_0$ . Then we obtain the rescaled equation for the order parameter  $\psi(x, t)$  of the following form (primes are omitted)

$$\partial_t \psi(\mathbf{r}, t) = \nabla^2 [-\varepsilon \psi + \psi^3 - \nabla^2 \psi + a \cos(qx)], \quad (53)$$

where

$$\varepsilon = \frac{T_c - T}{T_c - T_0}, \quad a = \frac{D_T}{D} \left( \frac{u}{|b|} \right)^{1/2} \phi_c (1 - \phi_c) \delta T_0. \quad (54)$$

Equation (53) describes the dynamics of phase separation in the presence of a spatially periodic forcing following a quench from the stable one-phase region ( $\varepsilon < 0$ ) to a reference temperature in the two-phase region ( $\varepsilon > 0$ ). In the following we will consider only the case of a symmetric quench with  $\int d\mathbf{r} \psi = 0$  as initial condition at  $t = 0$ .

In the absence of the forcing ( $a = 0$ ) the homogeneous solution  $\psi = 0$  becomes unstable for  $\varepsilon > 0$  against linear perturbations  $\sim \exp(\sigma t + i\mathbf{k} \cdot \mathbf{r})$  with wave number  $k \in (0, \sqrt{\varepsilon})$  and the growth rate  $\sigma = k^2(\varepsilon - k^2)$ . The most unstable (fastest growing) mode is characterized by  $k_m = \sqrt{\varepsilon/2}$  with  $\sigma_m = \varepsilon^2/4$ . If a two-dimensional system phase separating system the spatial extension in one direction is smaller than the wavelength of the fastest growing mode, it can be considered as a quasi one-dimensional systems.

### 6.1 Spatially periodic solutions and their stability

For positive values of the control parameter  $\varepsilon$ , stationary, spatially periodic solutions  $\psi_s(x) = \psi_s(x + 2\pi/q)$  of Eq. (53) may be found with and without forcing. However, in the case of a vanishing forcing amplitude ( $a = 0$ ) in Eq. (53) this equation has a  $\pm\psi$ -symmetry and therefore one has a pitchfork bifurcation from the trivial solution  $\psi = 0$  to finite amplitude periodic solutions as indicated in Fig. 19. However, in the unforced case periodic solutions of Eq. (53) are for any wave number  $q$  unstable against infinitesimal perturbations that induce coarsening processes [118, 113].

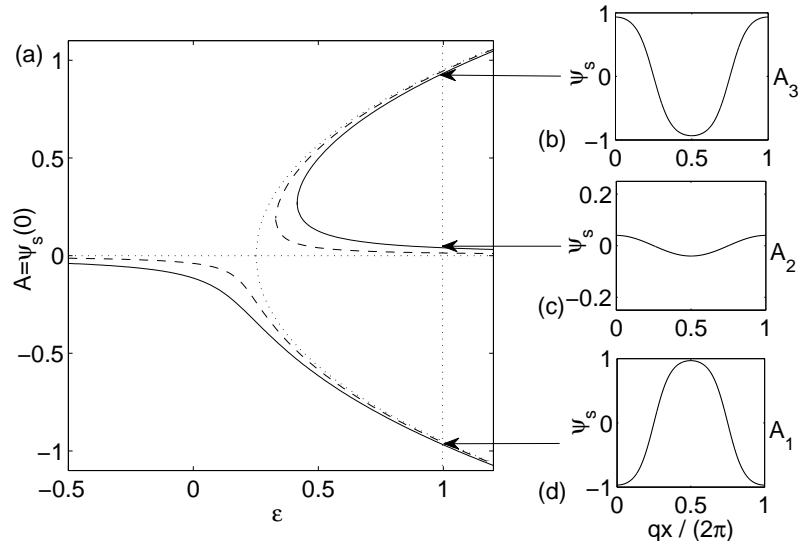


**Fig. 19** Part (a) shows the bifurcation diagram for spatially periodic solutions at a forcing wave number  $q = 0.5$  and modulation amplitudes  $a = 0$  (dotted),  $a = 0.01$  (dashed) and  $a = 0.03$  (solid). Parts (b), (c) and (d) show the three solutions  $\psi_s(x)$  over one period corresponding to the different branches of the bifurcation diagram for  $a = 0.03$  and  $\varepsilon = 1$ . Fig. from Ref. [119].

For finite values of the modulation amplitude  $a$  the broken  $\pm\psi$ -symmetry is indicated in Fig. 19 for  $a = 0.01$  by the dashed line and for  $a = 0.03$  by the solid

line. While we have in the unmodulated case a trivial solution  $\psi = 0$  and two finite solutions with identical amplitudes but of opposite sign, one finds in the forced case three periodic solutions,  $A_1$ ,  $A_2$  and  $A_3$ , of different amplitude as shown for one period in Fig. 19(b)-(d). These three different solutions have been determined by solving Eq. (56) by a Galerkin method, namely by expanding the solution  $\psi_s(x)$  with respect to periodic functions (Fourier series) and by solving the resulting non-linear equations for the amplitudes of the periodic expansion functions by a Newton method. The  $A_3$ - and  $A_2$ -solutions are in phase with the external modulation and the preferred  $A_1$ -solution is shifted by half a period. One should also note, that the  $A_1$  solution exists already in the range  $\varepsilon < 0$  and therefore in the one phase region without forcing.

Besides the existence of the periodic solutions  $\psi_s(x)$  of Eq. (53) one is also interested in their stability. For this purpose we use as ansatz a superposition of the stationary periodic solution  $\psi_s(x)$  and a time-dependent perturbation  $\psi_1(x, t)$

$$\psi(x, t) = \psi_s(x) + \psi_1(x, t) , \quad \psi_1(x, t) = e^{\sigma t} \phi(x) , \quad (55)$$

where  $\psi_s(x)$  satisfies the equation

$$-\varepsilon \psi_s + \psi_s^3 - \partial_{xx} \psi_s + a \cos(qx) = 0 \quad (56)$$

with periodic boundary conditions  $\psi_s(0) = \psi_s(2\pi/q)$ . Substituting (55) into Eq. (53) and linearizing this equation with respect to the perturbation  $\psi_1$  we arrive at a linear eigenvalue problem

$$\sigma \phi = \partial_{xx} \mathcal{L} \phi , \quad \mathcal{L} = -\varepsilon + 3\psi_s^2 - \partial_{xx} , \quad (57)$$

where  $\phi(x)$  can be represented in Floquet form

$$\phi(x) = e^{isx} \phi_F(x) . \quad (58)$$

Here  $s$  is the Floquet exponent and  $\phi_F(x)$  is  $2\pi/q$ -periodic. For a given  $\varepsilon > 0$  and  $q$  we are interested in the largest real part of  $\sigma(s, a)$  and therefore in the growth rate of the small perturbation  $\psi_1(x, t)$  with respect to each stationary periodic solution  $A_1$ ,  $A_2$  or  $A_3$ . The neutral stability condition  $\sigma(a, s, q) = 0$ , which separates the parameter range where the periodic solutions are stable from the unstable range, is a condition to determine the critical forcing amplitude  $\tilde{a}(s, q)$ . For forcing amplitudes larger than this the growth rate of the perturbation is negative and therefore the stationary periodic solutions  $\psi_s$  are stable with respect small perturbations  $\psi_1$ .

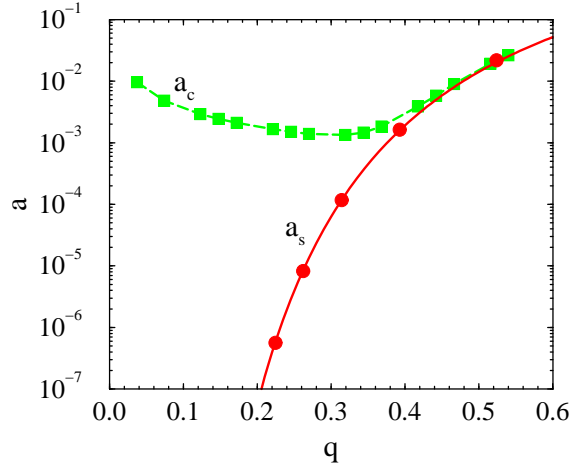
In the limit with wave numbers of the forcing small compared to the wave number of the fastest growing mode of the unforced system,  $q/k_m \ll 1$ , the stationary solution  $\psi_s$  can be determined and the neutral stability condition  $\sigma(a, s, q) = 0$  can be solved analytically in a perturbative way (see [113] for details). With the resulting analytical solution for  $A_1$  the following expression for the critical forcing amplitude is obtained:

$$a_s(s, q) = [1 + \cos(\pi s/q)] \varepsilon^{3/2} 32 (k_m/q) e^{-2\pi k_m/q} \left[ 1 + \frac{(\pi q/k_m)^2}{24} \right]. \quad (59)$$

Since the amplitude  $a_s$  takes its maximum in the limit  $s \rightarrow 0$ , the periodic solution  $A_1$  becomes at first unstable for long wavelength perturbations.

Similar as  $\psi_s(x)$  also  $\phi_F(x)$  is calculated by solving Eq. (57) by a Galerkin method and in general the neutral stability condition has to be solved numerically. We find in general, that the stationary solutions  $A_2$  and  $A_3$  are always unstable with respect to small perturbations. In Fig. 20 the forcing amplitude  $a_s(q)$ , as given by Eq. (59) for  $s = 0$ , is plotted (solid line) together with the corresponding numerical results (solid circles) and the deviations between both are tiny.

**Fig. 20** The forcing amplitude  $a_s$  above which the periodic solution  $A_1$  is linearly stable. The solid line is the approximate analytical result according to Eq. (59) and the solid circles are obtained numerically. The critical amplitude  $a_c$  above which the evolution of the initially homogeneous system after the quench is locked to the  $2\pi/q$ -periodicity of the forcing. The results are given for  $\varepsilon = 1$ .



The stability of two-dimensional stripe patterns that are periodic along the same direction (here the  $x$  direction) as the forcing has been investigated numerically. For this purpose we have chosen a similar ansatz as in one dimension,

$$\psi_1(x, y, t) = e^{\sigma t} e^{i(sx+py)} \phi_F(x), \quad (60)$$

but which depends now on two Floquet exponents:  $s$  ( $x$ -direction) and  $p$  ( $y$ -direction). The linear stability analysis shows, that additional transversal degrees of freedom do not influence the stability boundary  $a_s$ , cf. Fig. 20, as obtained in the case of the one-dimensional model.

As mentioned above, for finite forcing amplitudes one has already periodic  $A_1$  solutions in the range  $\varepsilon < 0$ . But, when the system is quenched into the two-phase region with  $\varepsilon > 0$ , where one may choose for reasons of simplicity  $\varepsilon = 1$ , the spinodal decomposition sets in and the late stage of the phase separation process depends on the forcing amplitude  $a$ . It is an interesting question, for which parameter combinations and independent of the initial conditions before the quench, the systems ends up in a  $A_1$  solution, that is locked to the periodicity of the external forcing?

The question has been investigated by numerical simulations of Eq. (53) in one spatial dimension with a typical system size  $L = 512$ . In order to test the results depend on their independence of the system size, we also made selected runs for  $L = 1024$  and  $2048$ . As initial condition we took small fluctuations around the homogeneous (single phase) state  $\psi = 0$  by assigning to each lattice site a random number uniformly distributed in the interval  $\pm 0.01$ . In order to average over random initial configurations 100 runs were performed for each parameter combination. Our simulations show that there is a well-defined critical amplitude  $a_c = a_c(q)$ , above which the time evolution of the system always ends up in the stationary  $A_1$  solution that is locked to the wavelength  $2\pi/q$  of the external forcing, independent of the initial conditions. In Fig. 20 the critical amplitude  $a_c(q)$  is shown (solid squares) as obtained from the numerical simulations ( $\varepsilon = 1$ ).

Since linear stability of the periodic solution of type  $A_1$  is a necessary condition for it being an attractor one has  $a_c(q) \geq a_s(q)$ . For  $q$  approaching the fastest growing wave number  $k_m = \sqrt{\varepsilon/2}$  one has  $a_c(q) \approx a_s(q)$  (see Fig. 20), which is actually not surprising, and this value gives a reasonable estimate for  $a_c(q)$  also for smaller values of  $q$ .

## 6.2 Traveling spatially periodic forcing

A spatiotemporal periodic forcing is a rather recent and interesting development for exploring various facets of pattern formation in systems with nonconserved order parameters [69, 70, 71, 72, 73]. A forcing traveling with the velocity  $v$  is also in systems with a conserved order parameter a further interesting possibility to explore various properties of phase separation dynamics. In particular, we consider the effects of traveling spatially periodic forcing in the framework of our extended Cahn-Hilliard model with thermodiffusion [see Eqs. (49), (50)]. Using dimensionless variables, as introduced by (52), the modified CH equation is given by

$$\partial_t \psi(\mathbf{r}, t) = \nabla^2 \{ -\varepsilon \psi + \psi^3 - \nabla^2 \psi + a \cos[q(x - vt)] \} . \quad (61)$$

The forcing term  $a \cos[q(x - vt)]$  is caused by an interplay between a traveling temperature modulation and thermodiffusion (Soret effect). Such a traveling spatially periodic temperature modulation could be created for instance in optical grating experiments [44, 87] with a light intensity of the form  $I(\mathbf{r}, t) \sim \cos[q(x - vt)]$ . Another possibility is to move a sample with a velocity  $v$  across a modulated temperature field. The control parameter  $\varepsilon$  in Eq. (61) corresponds to a dimensionless distance to the critical temperature of the binary mixture. Transformation of Eq. (61) in the frame comoving with the traveling forcing  $x \rightarrow x - vt$  gives

$$\partial_t \psi(\mathbf{r}, t) = \nabla^2 [ -\varepsilon \psi + \psi^3 - \nabla^2 \psi + a \cos(qx) ] + v \partial_x \psi . \quad (62)$$

As it was shown before, if phase separation is forced by a stationary and spatially periodic temperature modulation then the coarsening dynamics is interrupted above

some critical value of the forcing amplitude  $a$  and it is locked to the periodicity of the external forcing. However, if this forcing is “pulled” by a velocity  $v \neq 0$ , the traveling periodic solutions of Eq. (61) exist only in a certain range of  $v$  depending on  $a$ .

Thus we are interested in the conditions of the existence and stability of the spatially periodic solutions  $\psi_s(x) = \psi_s(x + 2\pi/q)$  of Eq. (62) in the comoving frame. The nonlinear solutions and the bifurcation diagram as given in Fig. 19 are only slightly changed by a small traveling velocity. However, with increasing values of  $v$  a phase shift  $\Delta\phi$  between the periodic forcing  $\sim \cos(qx)$  and the solution  $\psi_s(x)$  occurs. The maximum phase shift that can be achieved is about  $\Delta\phi_m = \pi/2$  at a certain velocity  $v_{ex}$  above which the solution does not exist. Consider  $\psi_s(x)$  being a  $2\pi/q$ -periodic solution of the following equation

$$\partial_{xx} [-\varepsilon\psi_s + \psi_s^3 - \partial_{xx}\psi_s + a\cos(qx)] + v\partial_x\psi_s = 0. \quad (63)$$

Equation (63) can be integrated twice and using the periodicity of  $\psi_s$  an integration of the resulting equation with respect to the interval  $(0, 2\pi/q)$  gives

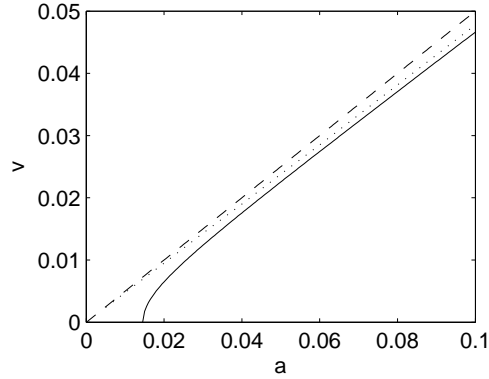
$$aq \int_0^{2\pi/q} \sin(qx)\psi_s(x)dx - v \int_0^{2\pi/q} \psi_s^2(x)dx = 0. \quad (64)$$

Clearly the maximum velocity  $v_{ex}$ , at which the periodic solution  $\psi_s$  still exists, corresponds to the solution which is shifted by  $\pi/2$  with respect to the forcing, i.e., for  $\psi_s \sim \sin(qx)$ .

The linear stability analysis of periodic solutions  $\psi_s(x)$  of Eq. (63) with respect to small perturbations have been performed numerically (see [119] for details). It has been found that the solutions  $A_2$  and  $A_3$  are again always unstable, whereas the  $A_1$ -solution can be stable in a certain range of the parameters. For given values of  $\varepsilon$  and  $q$  the modulation amplitude  $a$  has to exceed a certain value  $a_s(q)$  (see Fig. 20) to stabilize the  $A_1$ -solution. If the traveling velocity  $v$  is smaller than a critical one  $v_c(\varepsilon, a, q)$  the  $A_1$  solution remains stable. The critical velocity  $v_c(\varepsilon, a, q)$  is given by the solid line in Fig. 21 and for  $v > v_c(\varepsilon, a, q)$  the spatially periodic solution is linearly unstable. The onset of instability occurs for small values of the Floquet exponent  $s \rightarrow 0$ , i.e., it belongs to a long-wave perturbation as in the case of  $v = 0$ . In Fig. 21 also the boundary of the existence range of periodic solutions  $v_{ex}(\varepsilon, a, q)$  is shown as obtained approximately from Eq. (64) (dashed line) and by a full numerical simulation (dotted line). Since the stability boundary (solid line) always lies below  $v_{ex}$  the periodic solution always becomes unstable before the existence range is reached.

The temporal evolution of  $\psi(x, t)$  in the laboratory frame, as described by Eq. (61) in the 1D case, is shown in Fig. 22 for three regimes of the traveling forcing starting with the initial condition  $\psi = 0$  and superimposed with small noise. In Fig. 22(a) the velocity is sufficiently small and belongs to the range where the solution is locked to the traveling forcing. In Fig. 22(b) the velocity is chosen in the range  $v_c < v < v_{ex}$ , where the solution locked to the traveling forcing still exists,

**Fig. 21** Above the solid line the spatially periodic solution is unstable. The dashed line marks the existence boundary above which the spatially periodic solution does not exist due to the criterion given by Eq. (64). The dotted curve marks the existence boundary obtained numerically from Eq. (63). The parameters are  $\varepsilon = 1$  and  $q = 0.5$ .



but where it is linearly unstable. In this parameter range the solution is locked during the initial period of phase separation before coarsening takes over. In Fig. 22(c) the temporal evolution of phase separation is shown for  $v > v_{ex}$  where the locked solution does not exist anymore. At this velocity an interesting pinning-depinning behavior can be observed during the initial stage of phase separation. One still has a traveling periodic solution with the same wave number as the forcing but with a velocity smaller than the velocity of the forcing. Due to the velocity mismatch the phase shift between the solution and the forcing is slowly increased before it reaches about half of the forcing period. From that moment the periodic solution practically stops moving (pinning) until the forcing shifts over the next half of the period. After that the solution starts moving again (depinning) and the process repeats itself a few times. Later on the wavelengths of the solution and the forcing become different and the coarsening takes place.

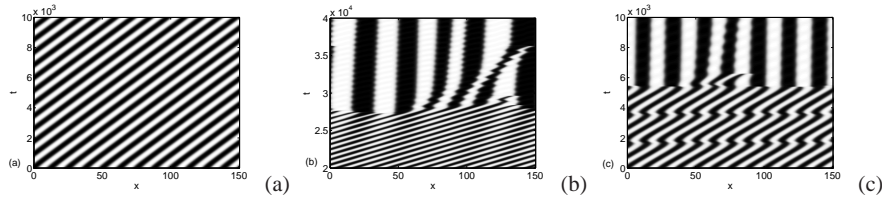


**Fig. 22** Temporal evolution of phase separation for  $v = 0.015 < v_c$  (a),  $v_c < v = 0.0185 < v_{ex}$  (b) and  $v = 0.02 > v_{ex}$  (c). The other parameters are  $\varepsilon = 1$ ,  $q = 0.5$ , and  $a = 0.04$ . Fig. from Ref. [119].

### 6.3 Periodic patterns in 2D

In two spatial dimensions phase separation can become more complex due to additional degrees of freedom and their consequences are investigated by extended simulations of Eq.(53) in two spatial dimensions and we have characterized the simulated patterns by the structure factor

$$S(\mathbf{k}, t) = |\hat{\psi}(\mathbf{k}, t)|^2, \quad \hat{\psi}(\mathbf{k}, t) = \int d\mathbf{r} e^{i\mathbf{k}\cdot\mathbf{r}} \psi(\mathbf{r}, t), \quad (65)$$

which can be also measured experimentally and allows direct comparison between experimental and theoretical results. For the unforced case (standard Cahn-Hilliard equation) the structure factor is isotropic  $S = S(|\mathbf{k}|, t)$  and possesses at long times the universal scaling behavior  $S(k, t) \sim l(t)^d G[kl(t)]$ , where the characteristic length of the domains evolves in time as  $l(t) \sim t^{1/3}$  (for  $d \geq 2$ ) [120]. By the spatially periodic forcing the rotational symmetry is broken in the plane and one may expect an anisotropy of the structure factor. The average domain length in the  $x$  and  $y$  directions can be related to the characteristic length scales

$$l_x(t) = [\langle k_x \rangle(t)]^{-1}, \quad l_y(t) = [\langle k_y \rangle(t)]^{-1}, \quad (66)$$

where

$$\langle k_x \rangle(t) = \frac{\int dk_x S(k_x, 0, t) k_x}{\int dk_x S(k_x, 0, t)}, \quad \langle k_y \rangle(t) = \frac{\int dk_y S(0, k_y, t) k_y}{\int dk_y S(0, k_y, t)}. \quad (67)$$

Numerical simulations of Eq. (53) were performed using central finite difference approximation of the spatial derivatives with 4-th order Runge-Kutta integration of the resulting ordinary differential equations in time. The typical system size was  $L_x = L_y = 256$ . Some test runs were made with  $L_x = L_y = 512$  and 1024. We used a uniform mesh size  $\delta x = \delta y = 1$  and time step  $\delta t = 2 \times 10^{-2}$ . The accuracy of calculations was checked by choosing  $\delta x = \delta y = 0.5$  and  $\delta t = 2 \times 10^{-3}$ . The dynamics of spinodal decomposition was computed over 6–7 decades in time, which allows monitoring the late stages of the phase separation process. Starting with random initial conditions with  $|\psi| < 0.01$ , the characteristic length dynamics was calculated by averaging over 100 runs.

Without driving ( $a = 0$ ) one has the typical scenario of spinodal decomposition and there is no anisotropy in the behavior of  $l_x$  and  $l_y$  (Fig. 23). Thus, small perturbations grow exponentially and at about  $t \sim 15$  (not shown) a nonlinear saturation of the fastest growing mode becomes important and sharp domain boundaries form. At about  $t \sim 30$  the late stage coarsening starts and we observe the well-known scaling  $l_x \sim l_y \sim t^{1/3}$ . In Fig. 24 snapshots of the phase separation process are presented for a particular run.

We have found that in the 2D case, similar to 1D, there exists a critical driving amplitude  $a_c$  above which the spinodal decomposition ends up in the stationary periodic solution with the period of the forcing, i.e., striped structure. The critical

**Fig. 23** Dynamics of the characteristic length scales  $l_x(t)$  and  $l_y(t)$  without forcing ( $a = 0$ ). System size  $L_x = L_y = 256$ ,  $\varepsilon = 1$ .

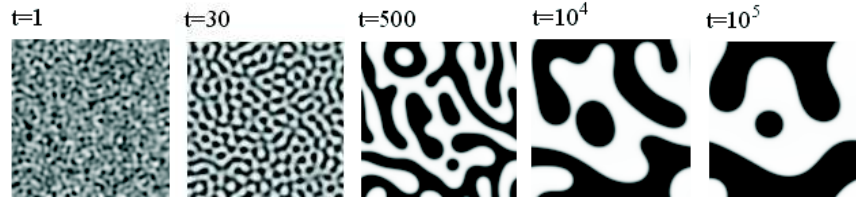
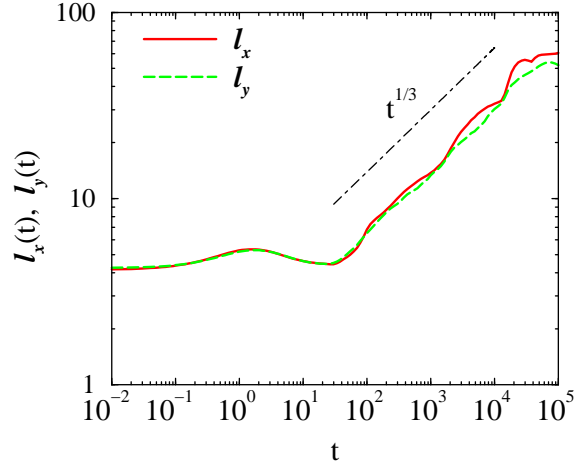
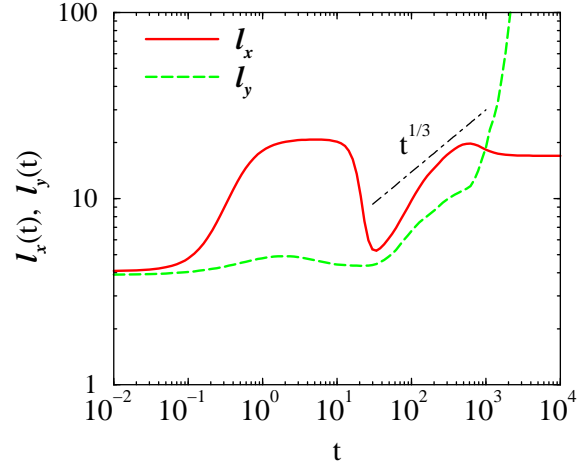


**Fig. 24** Snapshots of the phase separation process. The same parameters as in Fig. 23.

amplitude turned out to be about 3–5 times larger than in the one-dimensional case. In particular, for  $q = 6\pi/L_x$  with  $L_x = 256$  one has in 2D  $a_c = 0.014$  whereas for 1D  $a_c = 0.0045$ . Thus, for 2D the upper curve in Fig. 20 moves slightly upward (the linear stability curve  $a_s$  remains unchanged).

In Fig. 25 the dynamics of the characteristic length scales  $l_x$  and  $l_y$  is presented for the case  $a = 0.05 > a_c$  and in Fig. 26 typical snapshots are shown. The peculiar non-monotonic behavior of  $l_x$  at early times can be understood as follows: in the linear range the noise-initiated fastest mode grows exponentially as  $\psi_0 \exp(t/4)$  and the forced modulation with wave number  $q$  grows linearly as  $at$  (its exponential growth is small), see Eq. (53). Thus, shortly after the quench the fastest mode determines the average domain size. At a time  $t_1 = (\psi_0/a) \exp(t_1/4) \sim \psi_0/a = 0.2$  there is a crossover, beyond which the anisotropy becomes strong and  $l_x$  reaches a plateau that is controlled by the wave number of the forcing. Eventually, beyond  $t_2 = (\psi_0/a) \exp(t_2/4) \approx 18$ , the exponential growth of the fastest mode wins, which leads to a drop of  $l_x$ . Although at this time nonlinearities are already noticeable, the suppression of the effect of the forcing remains. Subsequently one has essentially isotropic coarsening until  $l_x$  saturates at  $1/q$ . After this ( $t > 500$ ) the ordering in the  $y$  direction becomes exponentially fast. Actually the late stage remains essentially unchanged if the forcing is turned on as late as  $t \sim 80$  where the average domain size

**Fig. 25** Dynamics of the characteristic length scales  $l_x(t)$  and  $l_y(t)$  for the driving amplitude  $a = 0.05$  well above the critical. System size  $L_x = L_y = 256$ ,  $\varepsilon = 1$ ,  $q = 6\pi/L_x$ .



has reached half the driving period. At a later time a forcing amplitude  $a = O(1)$  is needed to generate the periodic state.

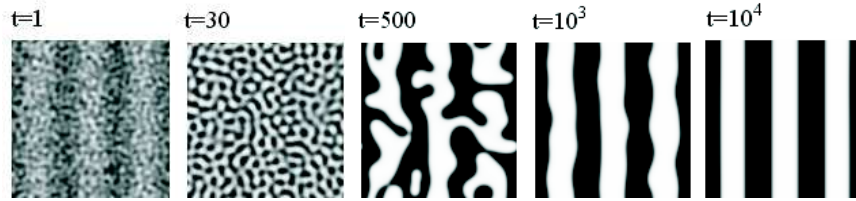


**Fig. 26** Snapshots of the phase separation process. The same parameters as in Fig. 25.

In Figs. 27, 28 we also show the dynamics of the characteristic length scales and snapshots for a driving amplitude slightly below the critical. One can see that at  $t \sim 10^3$  there is a competition between the influence of the forcing and the coarsening process, which finally wins.

The situation considered should be applicable to experiments on spinodal decomposition in sufficiently thin polymer films with small periodic temperature modulations created by means of optical grating technique or local laser heating. Then, for polymer blend layers of thickness less than a few micrometers the temperature variation across the film can be neglected for sufficiently small under cooling. Fig. 29(I) shows the time evolution of one single line written into a PDMS(16.4 kg/mol)/PEMS (22.0 kg/mol) blend ( $c = 0.512$  g/g,  $T_c = 314.7$  K,  $\alpha \approx 500$  m $^{-1}$ ) at a temperature 1.3 K below  $T_c$  and a laser power of 1 mW. The width of the laser focus is about 1.6  $\mu$ m, the length of the line is almost 140  $\mu$ m. Obviously, it is not possible to write a stable line into the sample. After approxi-

**Fig. 27** Dynamics of the characteristic length scales  $l_x(t)$  and  $l_y(t)$  for the driving amplitude  $a = 0.01$  slightly below the critical. System size  $L_x = L_y = 256$ ,  $\varepsilon = 1$ ,  $q = 6\pi/L_x$ .

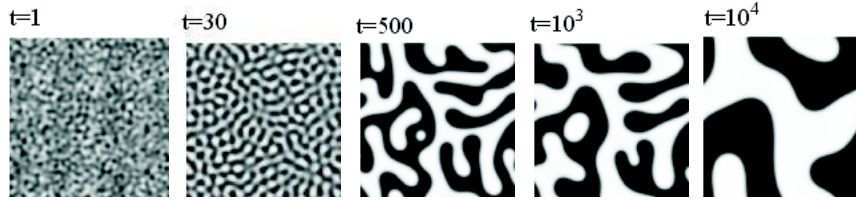
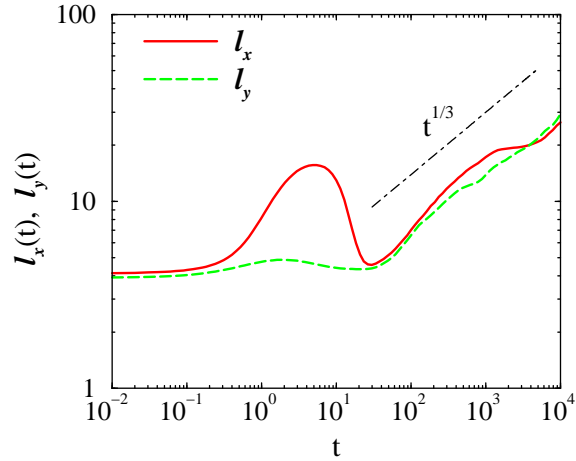


**Fig. 28** Snapshots of the phase separation process. The same parameters as in Fig. 27.

mately 1000 s surface tension effects lead to a pearling instability that eventually dominates the structure formation.

Fig. 29(II) shows the result if multiple parallel lines are written instead of a single one. A grid pattern evolves with a period comparable to the length scale of the already coarsened spinodal pattern. This grid pattern is stable as long as the writing process continues (A). Turning the laser off for 360 s leads to a beginning degradation (B), but continued writing again stabilizes the imposed structure (C). After turning the laser off again, some deformations due to bulging of the left- and right-most grid lines is observable (D). Continued writing of only the outermost (longer) lines allows for a continued stabilization of the central grid pattern (E). After switching the laser off, surface tension takes over and all parallel lines eventually decay into spherical structures.

## 7 Directional quenching

With directional quenching we present an effective mechanism to induce periodic stripe patterns in phase separating systems, where the wavelength of the patterns

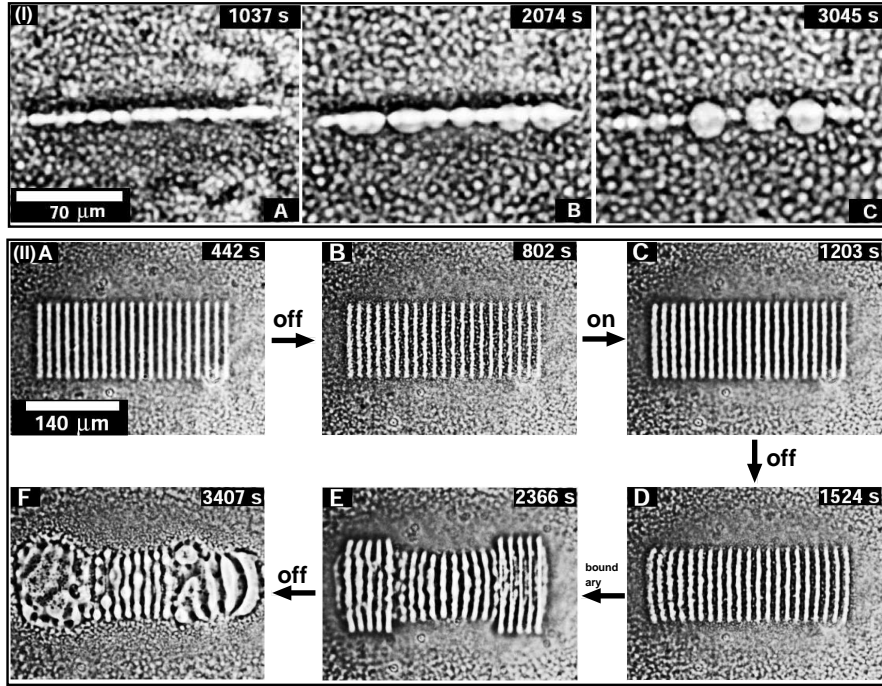


**Fig. 29** Temporal evolution of one single line (I) (written from  $t = 0$  s until  $t = 2074$  s at 1.3 K below  $T_c$ , laser-power 1 mW). 21 parallel lines (II) (written from  $t = 0$  s with 8 mW at 1.5 K below  $T_c$ ; “on” and “off” refer to switching of the laser; “boundary” means that only the outermost lines are written in order to stabilize the central part of the pattern; see text for details).

is uniquely selected by the velocity of a quench interface. If in addition a spatially periodic modulation of the quench interface is introduced also cellular patterns can be generated.

We choose again the generic Cahn-Hilliard model in one spatial dimension for describing phase separation [121, 122]

$$\partial_t \psi = \partial_{xx}(-\varepsilon \psi + \psi^3 - \partial_{xx} \psi), \quad (68)$$

where the real order parameter  $\psi(x, t)$  is a measure for the difference of the concentration of one component from its value at the critical point and  $\varepsilon$  is the control parameter. Here, in our first approach as in Ref. ??, thermodiffusion effects are neglected.

Directional quenching is achieved by changing  $\varepsilon$  from a negative value at  $x < x_q$  to a positive one for  $x > x_q$ , where the point  $x_q(t)$  moves in the laboratory frame with the velocity  $v$ .

$$\varepsilon(x, t) = \begin{cases} -\varepsilon, & x < -vt, \\ +\varepsilon, & x > -vt. \end{cases} \quad (69)$$

By this moving jump of the control parameter the system is divided into a stable and unstable region. Numerical simulations of the one-dimensional model in Eq. (68) and with the directional quenching (69) show that a periodic solution develops behind the quench interface in the unstable region. Typical examples for large and small values of the velocity  $v$  of the quench interface are shown in Fig. 30. For  $v$  above some critical value  $v^*$ , the periodic solution detaches from the moving quench interface and the wavelength of the solution becomes independent of  $v$ , cf. Fig. 30(a). In contrast, for  $v < v^*$  the solution remains attached to the quench interface and the wavelength is uniquely determined by  $v$ . Decreasing  $v$  the solution develops into a periodic kink lattice (sharp changes between  $\psi = \pm\sqrt{\varepsilon}$ ) where new kinks are continuously generated at  $x = x_q(t) = -vt$  [Fig. 30(b)]. The period of the

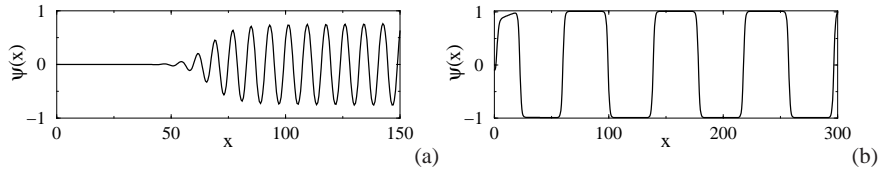
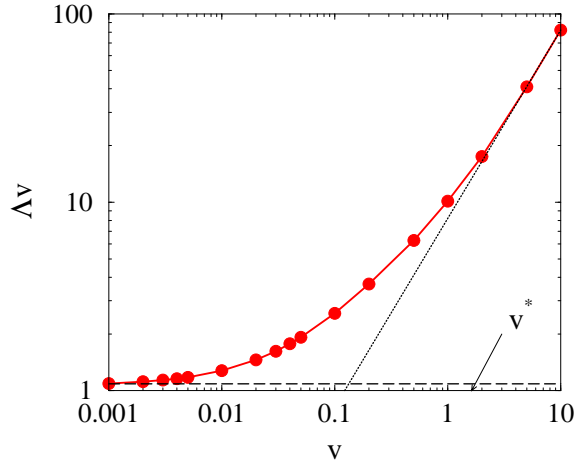


**Fig. 30** Solutions of Eq. (68) for  $\varepsilon = 1$  with the quench interface (69) in the comoving frame at  $x = 0$  for  $v = 2 > v^*$  in part (a) and for  $v = 0.02 \ll v^*$  in part (b). Only a part of the system of the total length  $l_x = 4096$  is shown. Figs. according to Ref. [123].

solution,  $\Lambda$ , turns out to be uniquely defined by the velocity of the quench interface, which is shown in Fig. 31. For  $v \rightarrow 0$  one has  $\Lambda \sim 1/v$  whereas for  $v > v^*$  one finds  $\Lambda = 2\pi/q^*$ . Although the periodic solutions far away from the moving quench inter-

**Fig. 31** Kink separation length  $\Lambda = 2\pi/q$  multiplied by the velocity  $v$  of the quench interface as a function of  $v$  (solid circles with a solid line as a guide to the eye);  $v^* = 1.622$  from Eq. (71). The dashed line corresponds to Eq. (72).  $\varepsilon = 1$  and Fig. according to Ref. [123].



face are in principle unstable against period doubling, the coarsening is extremely

slow for patterns generated with  $q \ll k_m$  [see Eq. (70)]. Thus the extension  $L_p$  of the (quasi-ideal) periodic solution behind the quench interface can be estimated as  $L_p = v\Delta t_p \approx v/\sigma_p$  where  $\sigma_p$  is the growth rate of the unstable period doubling mode given as [113, 118]:

$$\sigma_p = \varepsilon^2 16 \exp(-2\pi k_m/q) / (\pi k_m/q). \quad (70)$$

The two limiting cases of large and small values of the velocity  $v$  of the quench interface can be determined analytically. For large  $v$  we consider for instance the initial condition  $\psi = 0$  everywhere except a hump  $\psi > 0$  localized near  $x = 0$ . Then the time evolution of this initial perturbation is governed by the motion of wave fronts to the left and to the right with a well-defined velocity  $v^*$  and wave number  $q^*$ . These quantities can be calculated by a linear stability analysis of the leading edge of the front in the comoving frame [123]

$$v^* = \frac{\sqrt{7}+2}{3} \left( \frac{2}{3}(\sqrt{7}-1) \right)^{1/2} \varepsilon^{3/2}, \quad q^* = \frac{3(\sqrt{7}+3)^{3/2}}{8\sqrt{2}(\sqrt{7}+2)} \varepsilon^{1/2}. \quad (71)$$

The phase velocity and the wave number of the propagating periodic solutions, as obtained from the numerical simulations of Eq. (68), are in the range  $v > v^*$  independent on  $v$  and agree perfectly with  $v^*$  and  $q^*$  as given by Eq. (71). In the opposite limit  $v \rightarrow 0$  our starting point is a stationary solution of Eq. (68) for  $v = 0$  interpolating between  $\psi = 0$  at  $x < 0$  and  $\psi = \sqrt{\varepsilon}$  at  $x > 0$  and which is characterized by a sharp front at  $x \approx 0$ . If the quench interface according to Eq. (69) starts to move, the sharp front will follow at first. But since the spatial average  $\langle \psi \rangle$  is conserved, regions with  $\psi < 0$  have to be generated in the region  $x > x_q$ , which leads to the formation of a kink lattice [Fig. 30(b)]. The kink-lattice formation can be understood in terms of a fast switching stage and slow pulling stage: first a new kink is generated in a short time at  $x \approx x_q$ . During the slow stage this kink is pulled by the quench interface whereby its amplitude and the distance to the next kink behind increase until it exceeds some limiting value and then a new kink is generated. Repeating this process a regular kink lattice develops in the wake of the quench interface with the period  $\Lambda$ , which is uniquely determined by the velocity  $v$  of the moving quench interface (Fig. 31). The equilibrium period  $\Lambda$  can be calculated in the framework of boundary layer problem that gives [123]

$$\Lambda = \frac{4\sqrt{6}}{9} \frac{\varepsilon}{v} \approx 1.088 \frac{\varepsilon}{v}, \quad (72)$$

in perfect agreement with the results of numerical simulations in the limit  $v \rightarrow 0$  (Fig. 31).

The generalization of the analysis to the off-critical quench,  $\langle \psi \rangle \neq 0$ , is straightforward and the expressions (71) for  $v^*$  and  $q^*$  hold with the replacement  $\varepsilon \rightarrow \varepsilon - 3\langle \psi \rangle^2$ . In the limit  $v \rightarrow 0$  the distance  $\lambda_+$  between two kinks in the range  $\psi > 0$  becomes different compared to the kink-distance  $\lambda_-$  for  $\psi < 0$ . We find  $\lambda_+ - \lambda_- = \langle \psi \rangle \Lambda / \sqrt{\varepsilon}$  and for the resulting period  $\Lambda$  of the kink lattice,

$$\Lambda \equiv \lambda_+ + \lambda_- = \frac{2}{\nu} \left[ 2 \frac{\sqrt{6}}{9} \varepsilon + (8 - 25 \frac{\sqrt{6}}{9}) \langle \psi \rangle^2 \right]. \quad (73)$$

Similar as in case  $\langle \psi \rangle \neq 0$ , we have confirmed by numerical simulations of Eq. (68) the results in Eq. (73) for  $\langle \psi \rangle \neq 0$  in limit  $\nu \rightarrow 0$ .

Let us consider the 2D case  $\psi(x, y, t)$  where we study numerically the 2D version of the CH equation (68):

$$\partial_t \psi = \nabla^2 (-\varepsilon \psi + \psi^3 - \nabla^2 \psi) \quad (74)$$

with the moving quench interface (69). Zero flux boundary conditions have been used at  $x = 0, l_x$  and periodic boundary conditions at  $y = 0, l_y$ . Initially the quench interface is located at  $x_q = l_x$  moving from right to left. The system size was  $l_x = 512$ ,  $l_y = 256$  and we start with the homogeneous solution  $\psi = \langle \psi \rangle$  with small superimposed noise of the strength  $\delta \psi$  where  $\delta \psi \ll \sqrt{\varepsilon}$  and  $\delta \psi \ll \langle \psi \rangle$ . Thus the well-known Ginzburg criterion, necessary for the validity of a mean-field description of a phase separation process [5], is satisfied: in fact, the dynamics does not depend on the particular choice of  $\delta \psi$ .

In the case of the critical quench  $\langle \psi \rangle = 0$ , the orientation of the domains depends on the velocity of the quench interface [Fig. 32(a)-(c)]. At small  $\nu$  periodic patterns with domains perpendicular to the quench interface are formed [Fig. 32(a)]. Then for  $\nu$  above  $\nu_c \approx 0.45$  the 1D stripe patterns parallel to the quench interface appear [Fig. 32(b)-(c)]. Finally  $\nu > \nu^*$  leads eventually to irregular patterns similar to the case of a spatially homogeneous quench.

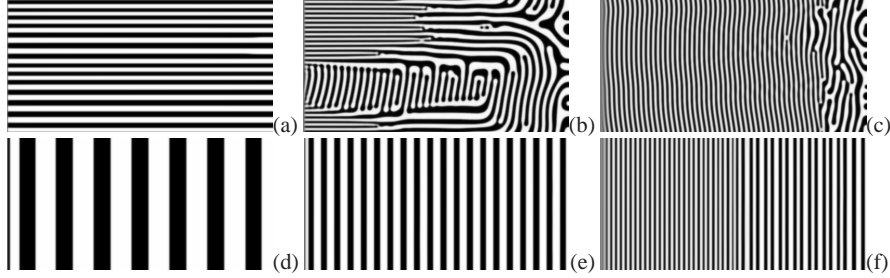


**Fig. 32** Snapshots of the phase separation in 2D at the time when the quench interface (69) ( $\varepsilon = 1$ ) almost reaches the left boundary.  $\langle \psi \rangle = 0$ :  $\nu = 0.01$  (a),  $\nu = 0.47$  (b), and  $\nu = 1$  (c).  $\langle \psi \rangle = 0.1$ :  $\nu = 0.02$  (d),  $\nu = 0.1$  (e), and  $\nu = 1$  (f).

In contrast, for the off-critical quench  $\langle \psi \rangle \neq 0$  when  $\nu < \nu^*$  always regular stripe patterns with domains parallel to the quench interface were found [Fig. 32(d)-(f)]. This situation is covered by an 1D analysis presented before where the period of the structure is uniquely determined by the velocity of the quench interface. In the limit  $\nu \rightarrow 0$  the period of the patterns found in our numerical simulations agree

with (73). For  $v > v^*$  irregular coarsening patterns similar to the case of a spatially homogeneous quench have been observed.

Finally we have studied the influence of a periodic modulation of the quench interface which reads as follows:

$$\varepsilon(x,y,t) = \begin{cases} -\varepsilon, & x < l_x + a \cos(py) - vt, \\ +\varepsilon, & x > l_x + a \cos(py) - vt. \end{cases} \quad (75)$$

In the case of a critical quench we found that the velocity  $v_c$  at which the transition from perpendicular stripe patterns [Fig. 33(a)] to parallel ones [Fig. 33(c)] occurs, depends on the modulation amplitude  $a$ . This dependence is very strong for values  $a$  of the order of the typical domain size at the initial stage of phase separation ( $a \sim \lambda_m = \pi/k_m$ ). Furthermore,  $v_c$  decreases with decreasing modulation wavenumber  $p$ . For  $p$  smaller than the wavenumber  $k_m$  of the fastest growing mode patterns with a cellular morphology forming behind the moving quench interface have been found [Fig. 33(b)].

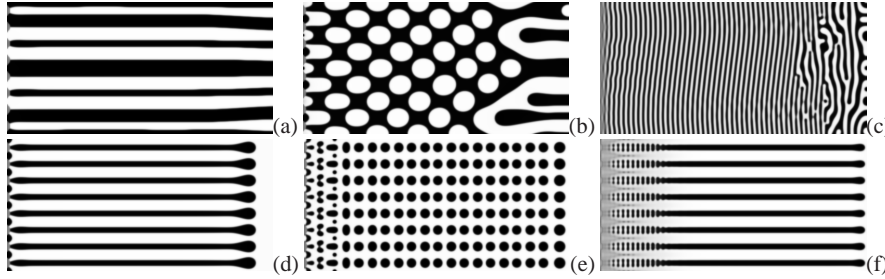


**Fig. 33** Snapshots of the phase separation in 2D at the time when the modulated quench interface (75) ( $\varepsilon = 1$ ,  $a = 4$ ,  $p = \pi/16$ ) almost reaches the left boundary.  $\langle \psi \rangle = 0$ :  $v = 0.01$  (a),  $v = 0.05$  (b), and  $v = 1$  (c).  $\langle \psi \rangle = 0.2$ :  $v = 0.05$  (d),  $v = 0.2$  (e), and  $v = 1$  (f).

In the case of an off-critical quench we found that  $\langle \psi \rangle \neq 0$  favors the formation of regular cellular planforms [Fig. 33(e)] at intermediate velocities of the quench interface, in analogy to the transition from perpendicular to parallel stripes for  $\langle \psi \rangle = 0$ .

Thus we have demonstrated that directional quenching in CH model leads to the formation of periodic solutions with the wavelength uniquely selected by the velocity of quench interface. Controlling phase separation by directional quenching turns out to be a promising tool to create regular structures in material science. Although slow coarsening cannot be avoided by directional quenching in principle, long lived periodic patterns can be “frozen in”, e.g., by a deep quench, induced polymerization, chemical treatment etc.

## 8 Summary and Conclusions

For critical and off-critical PDMS/PEMS polymer blends with an upper critical solution temperature  $T_c$  we investigated the coupling between an inhomogeneous temperature field and the order parameter, describing the local composition. In the asymptotic critical regime close to  $T_c$ , for  $\varepsilon = (T - T_c)/T_c < 0.02$ , the system belongs to the three-dimensional Ising universality class. Farther away from the critical point, for  $\varepsilon > 0.02$ , there is a crossover to the classical mean field behavior. Since the employed transient holographic grating technique works at significantly smaller  $q$ -values than typically encountered in photon correlation spectroscopy, the asymptotic critical scaling law of the diffusion coefficient  $D$  could be observed much closer to  $T_c$  without a conflict between the increasing correlation length  $\xi$  and the length scale defined by  $q^{-1}$ . A consistent description of  $D$  over a broad temperature range is based on a crossover model developed by Jacob and Kostko with an activation energy of the viscosity determined from the temperature dependence of the thermal diffusion coefficient  $D_T$  (Fig. 3). As predicted by Folk and Moser [124], the thermal diffusion coefficient  $D_T$  shows no critical slowing down and its temperature dependence can be described by a simple Arrhenius law with identical activation energies both for critical and off-critical mixtures. As a consequence of the insensitivity of  $D_T$  to the critical point and the critical slowing down of  $D$ , the Soret coefficient  $S_T = D_T/D$  of a critical blend diverges on approach of  $T_c$  with an exponent of  $-0.67$  in the asymptotic critical regime and with an exponent of  $-1$ , characteristic for the structure factor, in the mean field regime (Fig. 5).

Close to the critical point, the mixture becomes very susceptible to external perturbations, and only moderate temperature gradients are sufficient to induce significant concentration changes. The highest Soret coefficients measured exceed the values typically found for mixtures of organic solvents, consisting of small molecules, by four to five orders of magnitude. This high susceptibility of the order parameter opens the possibility for writing almost arbitrary composition patterns into a polymer blend by heating with a focused laser beam that can be scanned across the sample. These patterns can then be visualized by phase contrast or differential interference contrast microscopy. Because of the excursions along both the temperature and the concentration axes, a full numerical model requires as input the knowledge of both diffusion coefficients  $D$  and  $D_T$  over the entire concentration and temperature range of the homogeneous phase. The measured data have been interpolated within the framework of the pseudo-spinodal concept. These data are shown in Fig. 8, and PDMS/PEMS is up to now the only polymer blend where these coefficients are available not only for a critical composition but also for the entire one-phase regime.

Numerical modeling shows that very sharp and localized structures are formed during the initial linear growth regime, although the driving temperature profile has already reached its broadened stationary shape. This at a first sight surprising effect can be rationalized by recalling that the evolution of the concentration profile is driven by the Laplacian of  $T(\mathbf{r}, t)$  rather than the temperature itself. At later times,

solvent convection largely exceeds thermal convection and leads to asymmetric vertical cross sections of the patterns even for only  $100\ \mu\text{m}$  thick samples (Fig. 12).

The coupling of the order parameter to the temperature gradient also leads to unexpected excursions along the concentration axis in the case of off-critical mixtures. As a consequence, equilibrium phase diagrams lose their usual meaning in thermal nonequilibrium situations, and even an off-critical blend with a temperature above the binodal can be quenched into phase separation by local heating with a laser beam.

After crossing the spinodal from the homogeneous into the two-phase regime, spinodal decomposition sets in and leads to characteristic bicontinuous spinodal patterns with a characteristic length scale that grows during the coarsening stage. The strong Soret effect can not only be utilized to write composition patterns within the homogeneous phase but also opens a route for a controlled local manipulation of the spinodal decomposition patterns below  $T_c$  (Fig. 18). After switching the writing laser off, such an enforced perturbation freely evolves in time in competition with the coarsening dynamics of the unperturbed spinodal pattern.

Theoretically we have described in the framework of a generalized Cahn-Hilliard model effects of stationary and traveling spatially periodic temperature-modulations as well as the effects of moving quench interfaces on spinodal decomposition in binary fluid mixtures and polymer blends. In several phase separating systems, such as in polymer blends as investigated in this work also experimentally, thermodiffusion plays an important role in the presence of inhomogeneous temperature distributions. Since the model takes thermal diffusion into account we were able to reproduce the essential features of spatio-temporal dynamics observed in experiments on thermal patterning of polymer blends in the two-phase regime.

In such systems spatial temperature modulations may cause, via the thermodiffusion effect, concentration modulations in the composition of polymer blend already above the critical temperature, below which phase separation sets in. If the mean temperature crosses the critical temperature from above, phase separation sets in. However, a spatially periodic temperature modulation changes the phase separation process in polymer blends considerably.

If the modulation amplitude of the temperature exceeds a critical value, the spatially periodic forcing interrupts phase separation and the periodicity of the concentration modulation is locked to the wavelength of the temperature modulation. In the case of a traveling temperature-modulation the critical modulation amplitude required for locking the concentration modulation with respect to external forcing depends on the traveling velocity. One observes in a certain parameter range transient locking phenomena of the concentration modulations with respect to the external forcing. If the modulation amplitude is smaller than the critical one, the coarsening processes may be accelerated considerably by traveling temperature modulations in the two-phase regime.

For systems where thermodiffusive effects can be neglected, we have presented results on the effects of directional quenching where the control parameter jumps from above the critical temperature to below and where the location of the jump is moved by a finite velocity  $v$ . We have shown how by this method regular structures

are created in the process of phase separation behind the moving quench interface. Moreover, it was shown that the wavelength of periodic stripe patterns is uniquely selected by the velocity of the quench interface. If in addition a spatially periodic modulation of the quench interface is introduced also cellular patterns can be generated.

## Acknowledgement

We thank G. Meier and I. Alig for inspiring discussions and T. Wagner and G. Meier for providing part of the samples. The theoretical part of this work was originally initiated by L. Kramer (†). Essential parts of the work have been performed during the PhD-theses of W. Enge, A. Voit, M. Hartung and F. Schwaiger and the diploma theses of S. Frank and V. Weith. The work was supported by the Deutsche Forschungsgemeinschaft via the Collaborative Research Center SFB481.

## References

1. J.V. Sengers, Ber. Bunsenges. Phys. Chem. **76**, 234 (1976)
2. E.D. Siggia, B.I. Halperin, P.C. Hohenberg, Phys. Rev. B **13**, 2110 (1976).
3. P.C. Hohenberg, B.I. Halperin, Rev. Mod. Phys. **49**, 435 (1977)
4. K. Binder, Adv. Polym. Sci. **112**, 181 (1994)
5. K. Binder, J. Chem. Phys. **79**, 6387 (1983)
6. H. Sato, N. Kuwahara, K. Kubota, Phys. Rev. E **50**, R1752 (1994)
7. W. Theobald, G. Meier, Phys. Rev. E **51**, 5776 (1995).
8. G. Meier, B. Momper, E.W. Fischer, J. Chem. Phys. **97**, 5884 (1992)
9. W. Mayer, S. Hoffmann, G. Meier, I. Alig, Phys. Rev. E **55**, 3102 (1997)
10. S. Eckert, G. Meier, I. Alig, Phys. Chem. Chem. Phys. **4**, 3743 (2002)
11. S. Eckert, S. Hoffmann, G. Meier, I. Alig, Phys. Chem. Chem. Phys. **4**, 2594 (2002)
12. S. Eckert-Kastner, G. Meier, I. Alig, Phys. Chem. Chem. Phys. **5**, 3202 (2003)
13. H. Mao, C. Li, Y. Zhang, D.E. Bergbreiter, P.S. Cremer, J. Am. Chem. Soc. **125**, 2850 (2003)
14. M. Yamamura, S. Nakamura, T. Kajiwara, H. Kage, K. Adachi, Polymer **44**, 4699 (2003)
15. D. Jasnow, J. Viñals, Phys. Fluids **8**, 660 (1996)
16. K.W.D. Lee, P.K. Chan, X. Feng, Macromol. Theory Simul. **11**, 996 (2002)
17. K.W.D. Lee, P.K. Chan, X. Feng, Macromol. Theory Simul. **12**, 413 (2003)
18. P. Kolodner, H. Williams, C. Moe, J. Chem. Phys. **88**, 6512 (1988)
19. A. Königer, B. Meier, W. Köhler, Philos. Mag. **89**, 907 (2009).
20. C. Debuschewitz, W. Köhler, Phys. Rev. Lett. **87**, 055901 (2001).
21. G. Wittko, W. Köhler, J. Chem. Phys. **123**, 014506 (2005).
22. P.A. Artola, B. Rousseau, Phys. Rev. Lett. **98**, 125901 (2007)
23. R. Kita, G. Kircher, S. Wiegand, J. Chem. Phys. **121**, 9140 (2004).
24. G. Wittko, W. Köhler, Europhys. Lett. **78**, 46007 (2007).
25. S. Iacopini, R. Rusconi, R. Piazza, Eur. Phys. J. E **19**, 59 (2006).
26. R. Piazza, S. Iacopini, B. Triulzi, Phys. Chem. Chem. Phys. **6**, 1616 (2004)
27. D. Stadelmaier, W. Köhler, Macromolecules **41**, 6205 (2008).
28. M. Zhang, F. Müller-Plathe, J. Chem. Phys. **125**, 124903 (2006).
29. B.J. de Gans, R. Kita, S. Wiegand, J. Luettmer-Strathmann, Phys. Rev. Lett. **91**, 245501 (2003)

30. M.E. Schimpf, J.C. Giddings, J. Polym. Sci.: Part B: Polym. Phys. **27**, 1317 (1989).
31. P. Rossmanith, W. Köhler, Macromolecules **29**, 3203 (1996)
32. A. Ryskin, H.W. Müller, H. Pleiner, Physica D **submitted** (2002)
33. J. Luettmer-Strathmann, J. Chem. Phys. **119**, 2892 (2003)
34. J. Lenglet, A. Bourdon, J.C. Bacri, G. Demouchy, Phys. Rev. E **65**, 031408 (2002).
35. B. Hoffmann, W. Köhler, M. Krekhova, J. Chem. Phys. **118**, 3237 (2003).
36. R. Piazza, A. Guarino, Phys. Rev. Lett. **88**, 208302 (2002)
37. D. Braun, A. Libchaber, Phys. Rev. Lett. **89**, 188103 (2002)
38. J.K.G. Dhont, W.J. Briels, Eur. Phys. J. E **25**, 61 (2008).
39. J.K.G. Dhont, S. Wiegand, S. Duhr, D. Braun, Langmuir **23**, 1674 (2007).
40. J.K.G. Dhont, J. Chem. Phys. **120**, 1642 (2004)
41. J.K.G. Dhont, J. Chem. Phys. **120**(3), 1632 (2004)
42. G. Thomaes, J. Chem. Phys. **25**, 32 (1956)
43. M. Giglio, A. Vendramini, Phys. Rev. Lett. **34**, 561 (1975)
44. S. Wiegand, W. Köhler, in *Thermal Nonequilibrium Phenomena in Fluid Mixtures*, ed. by W. Köhler, S. Wiegand (Springer, Heidelberg, 2002), p. 189
45. D.W. Pohl, Phys. Lett. A **77**, 53 (1980).
46. S. Buil, J.P. Delville, E. Freysz, A. Ducasse, Opt. Lett. **23**, 1334 (1998)
47. J.P. Delville, C. Lalaude, A. Ducasse, Physica A **262**, 40 (1999)
48. M.C. Cross, P.C. Hohenberg, Rev. Mod. Phys. **65**, 851 (1993).
49. A.J. Bray, Adv. Phys. **43**, 357 (1994)
50. J. Vörös, T. Blättler, T. M., MRS Bull. **30**, 202 (2005)
51. H. Siringhaus, Adv. Mater. **17**, 2411 (2005)
52. T. Hashimoto, K. Matsuzaka, E. Moses, A. Onuki, Phys. Rev. Lett. **74**, 126 (1996).
53. Z. Chen, J. Kornfeld, S. Smith, J. Grothaus, M. Satkowski, Science **277**, 1248 (1997).
54. Y. Jayalakshmi, B. Khalil, D. Beysens, Phys. Rev. Lett. **69**, 3088 (1992)
55. M. Böltau, S. Walheim, J. Mlynek, G. Krausch, U. Steiner, Nature **391**, 877 (1998)
56. T. Hashimoto, J. Bodycomb, Y. Funaki, K. Kimishima, Macromolecules **32**, 952 (1999).
57. R. Sigel, G. Fytas, N. Vainos, S. Pispas, N. Hadjichristidis, Science **297**, 66 (2002)
58. B. Loppinet, E. Somma, N. Vainos, G. Fytas, J. Am. Chem. Soc. **127**, 9678 (2005)
59. B.P. Lee, J.F. Douglas, S.C. Glotzer, Phys. Rev. E **60**, 5812 (1999)
60. R.E. Kelly, D. Pal, J. Fluid Mech. **86**, 433 (1978)
61. M. Lowe, J.P. Gollub, T. Lubensky, Phys. Rev. Lett. **51**, 786 (1983)
62. P. Couillet, P. Huerre, Physica D **23**, 27 (1986)
63. P. Couillet, D. Walgraef, Europhys. Lett. **10**, 525 (1989)
64. W. Zimmermann, A. Ogawa, S. Kai, K. Kawasaki, T. Kawakatsu, Europhys. Lett. **24**, 217 (1993)
65. G. Hartung, F.H. Busse, I. Rehberg, Phys. Rev. Lett. **66**, 2742 (1991)
66. W. Zimmermann, R. Schmitz, Phys. Rev. E **53**, R1321 (1996)
67. R. Schmitz, W. Zimmermann, Phys. Rev. E **53**, 5993 (1996)
68. A.L. Lin, M. Bertram, K. Martinez, H.L. Swinney, A. Ardelea, G.F. Carey, Phys. Rev. Lett. **84**, 4240 (2000)
69. C. Utzny, W. Zimmermann, M. Bär, Europhys. Lett. **57**, 113 (2002)
70. D.G. Míguez, E.M. Nicola, A.P. Munuzuri, J. Casademunt, F. Sagues, L. Kramer, Phys. Rev. Lett. **93**, 048303 (2004)
71. S. Schuler, M. Hammele, W. Zimmermann, Eur. Phys. J B **42**, 591 (2004)
72. S. Rüdiger, D.G. Míguez, A.P. Munuzuri, F. Sagués, J. Casademunt, Phys. Rev. Lett. **90**, 128301 (2003)
73. S. Rüdiger, E.M. Nicola, J. Casademunt, L. Kramer, Phys. Rep. **447**, 028302 (2007)
74. H. Tanaka, T. Sigezuki, Phys. Rev. Lett. **75**, 874 (1995)
75. J. Kumaki, T. Hashimoto, S. Granick, Phys. Rev. Lett. **77**, 1990 (1996)
76. S.R. de Groot, P. Mazur, *Non-equilibrium thermodynamics* (Dover, New York, 1984)
77. L.D. Landau, E.M. Lifshitz, *Fluid Mechanics* (Pergamon, Oxford, 1987)
78. M. Hartung, A detailed treatment of the measurement of transport coefficients in transient grating experiments. Ph.D. thesis, Univ. Bayreuth (2007)

79. J. Luettmer-Strathmann, in *Thermal Nonequilibrium Phenomena in Fluid Mixtures*, ed. by W. Köhler, S. Wiegand (Springer, Heidelberg, 2002), p. 24
80. P.G. de Gennes, *Scaling concepts in polymer physics* (Cornell University Press, London, 1979)
81. W. Enge, W. Köhler, Phys. Chem. Chem. Phys. **6**, 2373 (2004).
82. W. Enge, W. Köhler, ChemPhysChem **5**, 393 (2004).
83. D. Schwahn, G. Meier, K. Mortensen, S. Janßen, J. Phys. II France **4**, 837 (1994)
84. S. Enders, A. Stammer, B. Wolf, Macromol. Chem. Phys. **197**, 2961 (1996)
85. K. Thyagarajan, P. Lallemand, Opt. Commun. **26**, 54 (1978)
86. W. Köhler, J. Chem. Phys. **98**, 660 (1993).
87. G. Wittko, W. Köhler, Philos. Mag. **83**, 1973 (2003).
88. W. Köhler, P. Rossmanith, J. Phys. Chem. **99**, 5838 (1995).
89. L. Kador, R. Bausinger, A. Leopold, D. Haarer, W. Köhler, J. Phys. Chem. A **108**, 1640 (2004).
90. M. Hartung, W. Köhler, Eur. Phys. J. E **17**, 165 (2005).
91. W. Enge, Thermodiffusion in polymermischungen. Ph.D. thesis, Univ. Bayreuth (2004)
92. H. Sato, N. Kuwahara, K. Kubota, Phys. Rev. E **53**, 3854 (1996)
93. K. Kawasaki, Ann. Phys. **61**, 1 (1970)
94. J. Jakob, M.A. Anisimov, J.V. Sengers, V. Dechabo, I.K. Yudin, R.W. Gammon, Appl. Optics **40**, 4160 (2001)
95. A.F. Kostko, M.A. Anisimov, J.V. Sengers, Phys. Rev. E **66**, 020803 (2002)
96. W. Enge, W. Köhler, Eur. Phys. J. E **15**, 265 (2004).
97. J. Rauch, W. Köhler, Macromolecules **38**, 3571 (2005).
98. H. Nakayama, O. Sugihara, N. Okamoto, Appl. Phys. Lett. **71**(14), 1924 (2006)
99. A. Voit, A. Krekhov, W. Köhler, Phys. Rev. E **76**, 011808 (2007).
100. B. Chu, F.J. Schoenes, M.E. Fisher, Phys. Rev. **185**, 219 (1969)
101. R. Beyer, *Handbuch der Mikroskopie*, 2nd edn. (VEB Verlag Technik, Berlin, 1977)
102. M. Born, E. Wolf, *Principles of optics* (Cambridge Univ. Press, New York, 1998)
103. C.J. Bellair, C.L. Curl, B.E. Allman, P.J. Harris, A. Roberts, L.M.D. Delbridge, K.A. Nugent, J. Microscopy **214**, 62 (2004)
104. A. Voit, Photothermische strukturierung binärer Polymermischungen. Ph.D. thesis, Univ. Bayreuth (2007)
105. G. Meier, D. Vlassopoulos, G. Fytas, Europhys. Lett. **30**, 325 (1995)
106. J. Rauch, M. Hartung, A.F. Privalov, W. Köhler, J. Chem. Phys. **126**, 214901 (2007).
107. M. Hartung, J. Rauch, W. Köhler, J. Chem. Phys. **125**, 214904 (2006).
108. J. Rauch, W. Köhler, J. Chem. Phys. **119**, 11977 (2003).
109. J. Rauch, W. Köhler, Phys. Rev. Lett. **88**, 185901 (2002).
110. F. Schwaiger, Ph.D. thesis, University of Bayreuth (2010)
111. A. Voit, A. Krekhov, W. Köhler, Macromolecules **40**, 9 (2007).
112. J.C. Meredith, A. Karim, E.J. Amis, Macromolecules **33**, 5760 (2000).
113. A.P. Krekhov, L. Kramer, Phys. Rev. E **70**, 061801 (2004).
114. F.S. Bates, G.D. Wignall, W.C. Koehler, Phys. Rev. Lett. **55**, 2425 (1985).
115. P. Guenoun, R. Gastaud, F. Perrot, D. Beysens, Phys. Rev. A **36**, 4876 (1987).
116. A. Voit, A. Krekhov, W. Enge, L. Kramer, W. Köhler, Phys. Rev. Lett. **94**, 214501 (2005).
117. M. Hammele, W. Zimmermann, Phys. Rev. E **73**, 066211 (2006).
118. J.S. Langer, Ann. Phys. (N.Y.) **65**, 53 (1971)
119. V. Weith, A. Krekhov, W. Zimmermann, Eur. Phys. J. B **67**, 419 (2009).
120. J.D. Gunton, M. San Miguel, P.S. Sahni, *Phase transitions and critical phenomena* (Academic, London, 1983), vol. 8
121. J.W. Cahn, J. e. Hilliard, J. Chem. Phys. **28**, 258 (1958).
122. J.W. Cahn, J.E. Hilliard, J. Chem. Phys. **31**, 688 (1959).
123. A. Krekhov, Phys. Rev. E **79**, 035302(R) (2009).
124. R. Folk, G. Moser, Phys. Rev. E **58**, 6246 (1998)